WinApclas, A Windows program for apatite supergroup minerals

Fuat Yavuz [1],*, Vural Yavuz [2]

[1] Department of Geological Engineering, Istanbul Technical University, 34469 Maslak, Istanbul, Turkey
[2] Department of Civil Engineering, Turkish-German University, 34820 Beykoz, Istanbul, Turkey

ABSTRACT

A Microsoft® Visual Basic software, called WinApclas, has been developed to calculate and classify wet chemical and electron-microprobe apatite supergroup mineral analyses based on the New Minerals, Nomenclature and Classification (CNMMN) of the International Mineralogical Association (IMA-10) nomenclature scheme. The program evaluates the 47 approved species based on the dominant cations at the M and T sites and anions at the X site in the reduced general formula $^{IX}M1_2{}^{VII}M2_3(^{IV}TO_4)_3X$ within the apatite, hedyphane, belovite, britholite and ellestadite groups. Mineral analyses of the apatite supergroup species are calculated with different estimation and normalization options including 13 total anions, 8 total (M+T=8), 3T (P+As+V+Si+S=3), 8 total (M=5 and T=3) and 5M cations, respectively. Using the calculated anion values of apatite supergroup mineral analyses, the program first allocates the T site cations with charges between +4 and +6 and then shares all remaining cations with smaller ones in the range of +1 to +3 to fill the M site. Considering the dominant M and T site anions, WinApclas determines the apatite supergroups and defines the species in each group according to the dominant valance and constituents on the basis of dominant X anion such as F⁻, Cl⁻ and OH⁻. The program allows the users to enter total 79 input variables that 54 of them (wt%) are used for the calculation and classification of apatite supergroups minerals, two of them (wt%) belonging to the melt or whole-rock SiO_2 and P_2O_5 compositions to be used in estimation of the apatite saturation temperature values (oC) and the rest 23 for apatite trace (ppm) and rare earth element (REE) contents to handle the compositional and discrimination plots for provenance and mineral exploration studies. By applying the semi-quantitative formulae for apatite mineral analyses, WinApclas also provides the user to estimate the F, Cl and relative S contents (ppm) of melts as well as the redox states of magmas. All the calculated values are stored in an output Microsoft® Excel file that can be used for further evaluations. WinApclas is distributed as a self-extracting setup file, including the necessary support files used by program, a help file, and representative sample data files.

Keywords: apatite; hedyphane; belovite; britholite; ellestedite; discrimination; provenance; software.

INTRODUCTION

The apatite supergroup consisting of phosphates, arsenates, vanadates, silicates and sulphates includes currently 47 species with a generic reduced (i.e., *Z*=2) general formula $^{IX}M1_2{}^{VII}M2_3(^{IV}TO_4)_3X$, which is commonly accepted by the mineralogical literature (Pasero et al., 2010). Their crystal structures, based on a heteropolyhedral framework of metal cations (M), tetrahedrally coordinated (T) atoms and columns of the additional X anions, provide a wide range of ions into the

five crystal-chemical groups including apatite, hedyphane, belovite, britholite and ellestadite (Pasero et al., 2010; Szuszkiewicz et al., 2018). Consequently, abundance of diverse ions hosted at the M (e.g., Ca^{2+}, Pb^{2+}, Ba^{2+}, Sr^{2+}, Mn^{2+}, Na^+, Ce^{3+}, La^{3+}, Y^{3+}, Bi^{3+}), T (e.g., P^{5+}, As^{5+}, V^{5+}, Si^{4+}, S^{6+}, B^{3+}) and X (e.g., F^-, Cl^-, and OH^-) sites in the apatite supergroup enable a large number of chemical compositions with distinct mineral species in the Earth's crust that commonly occur in all geological environments (Pasero et al., 2010; Bačík et al., 2020). The apatite group constitutes one of the most widespread and important phosphate, arsenate and vanadate minerals among the apatite supergroup species. Apatite group minerals are important minerals in rocks of igneous, hydrothermal, metamorphic and sedimentary origin. As apatite, with the general formula $Ca_5(PO_4)_3(F,Cl,OH)$, is a very common accessory mineral in magmatic rocks, ore deposits (e.g., porphyry Cu±Mo±Au) and biominerals (i.e., as constituents of the mammals' bones) its composition is considered a powerful tool for geochemical and petrological researches in tracing the origin and evolution of geological systems as well as the genesis of ore deposits (Rukhlov et al., 2016; Teiber et al., 2015; Chen et al., 2021; Chew et al., 2021; Kasatkin et al., 2023). On the other hand, apatite's widespread distribution in crystalline rocks with variable REE (i.e., La to Lu) and trace element (e.g., Sr, Mn, Y, U, Th, etc.) contents as well as its application in various dating techniques based on the decay of the radioisotopes U and Th provides specific provenance determinations and discrimination plots that can be used as a useful tool for the identification of the apatite source rocks and genetic types of apatite-bearing ore deposits (Belousova et al., 2002; Morton and Yaxley, 2007; Rukhlov et al., 2016; Mao et al., 2016; Andersson et al., 2019; O'Sullivan et al., 2020).

Although various computer programs for the calculation and classification of rock-forming silicate and associated accessory minerals have been published over the past two decades (e.g., Yavuz, 2001, 2003, 2007, 2013; Yavuz et al., 2014, 2015; Yavuz and Yıldırım, 2018, 2020; Yavuz and Yavuz, 2023, in press), software on the calculation and classification of apatite supergroup minerals, according to the current IMA report, has not yet been appeared in the literature. Taking this situation into consideration, in this paper, a computer program, called WinApclas, has been developed by using the Microsoft® Visual Basic programming language to calculate multiple apatite supergroup mineral data, up to 200 analyses at a time, obtained from both wet chemical and electron-microprobe techniques. The program estimates and classifies mineral analyses of the apatite supergroup on the basis of 13 total anions (apfu) with optional 8 total (M+T), 3 T and 5 M cations calculation and normalization procedures. Evaluations of

apatite supergroup mineral analyses by WinApclas are carried out based on the current IMA report (Pasero et al., 2010) considering the recently IMA-approved new species later than that report. WinApclas allows the user to display apatite supergroup minerals in several binary and ternary classification and compositional diagrams by using the Golden Software's Grapher program.

APATITE SUPERGROUP MINERALS NOMENCLATURE

Currently, the 47 valid minerals of the apatite supergroup are classified based on their crystal-chemical arguments in terms of the dominant M, T and X site ions in the reduced $^{IX}M1_2$ $^{VII}M2_3(^{IV}TO_4)_3X$ general formula, where the left superscripts indicate the ideal coordination numbers. Apatite (i.e., fluorapatite, chlorapatite and hydroxyapatite compositions herein), the most widespread species of this supergroup, has a robust hexagonal atomic framework consisting of two distinct metal-cation sites (M1, M2), a tetrahedral-cation site (T) and an anion column along four edges of the unit cell which incorporate more than half of the long-lived elements in their flexible structure that allow a wide degree of substitutions among cations (Pasero et al., 2010; Hughes and Rakovan, 2015). The IMA-approved mineral species within the apatite supergroup have been divided into five groups by Pasero et al. (2010) as follows (see Table 1):

(1) Apatite group: Consisting of hexagonal and pseudo-hexagonal phosphates, arsenates, and vanadates species (e.g., apatite, mimetite and vanadinite) with the same prevailing cation at both the M1 and M2 sites.

(2) Hedyphane group: Consisting of hexagonal and pseudo-hexagonal phosphates, arsenates and sulphates species (e.g., parafiniukite, hedyphane and cesanite) with different prevailing cations at the M1 and M2 sites.

(3) Belovite group: Consisting of hexagonal and trigonal phosphates species (e.g., belovite-(La), kuannersuite-(Ce) and fluorcaphite) that the M1 site split into the M1 and M1' sites with different prevailing cations.

(4) Britholite group: Consisting of hexagonal and pseudo-hexagonal silicates species (e.g., britholite-(Ce), tritomite-(Y) and fluorcalciobritholite) typically with partially ordered M1 and M2 cations.

(5) Ellestadite group: Consisting of hexagonal and pseudo-hexagonal sulphato-silicates species (e.g., chlorellestadite, hydroxylellestadite and mattheddleite) with the ideal ratio $(SiO_4)^{4-}:(SO_4)^{2-}=1:1$.

Although the correct placement of a species within the apatite supergroup can be a difficult procedure due to the ordering that require a high-quality crystal structure refinement, Pasero et al. (2010) proposed a series of following suggestions for apatite supergroup mineral analyses obtained from electron-microprobe

Table 1. A list of the 47 IMA-approved species in the apatite supergroup (revised from Pasero et al. 2010) classified by the WinApclas program.

Row	Apatite group	Symbol	M	T	X
1	Alforsite	Afr	Ba_5	$(PO_4)_3$	Cl
2	Chlorapatite	Clap	Ca_5	$(PO_4)_3$	Cl
3	Fluoralforsite§	Fafr	Ba_5	$(PO_4)_3$	F
4	Fluorapatite	Fap	Ca_5	$(PO_4)_3$	F
5	Fluorpyromorphite§	Fpym	Pb_5	$(PO_4)_3$	F
6	Hydroxylapatite	Hap	Ca_5	$(PO_4)_3$	(OH)
7	Hydroxylpyromorphite§	Hpm	Pb_5	$(PO_4)_3$	(OH)
8	Johnbaumite	Jbm	Ca_5	$(AsO_4)_3$	(OH)
9	Mimetite	Mim	Pb_5	$(AsO_4)_3$	Cl
10	Pieczkaite§	Pzk	Mn_5	$(PO_4)_3$	Cl
11	Pliniusite§	Pli	Ca_5	$(VO_4)_3$	F
12	Pyromorphite	Pym	Pb_5	$(PO_4)_3$	Cl
13	Stronadelphite	Sad	Sr_5	$(PO_4)_3$	F
14	Svabite	Sva	Ca_5	$(AsO_4)_3$	F
15	Turneaureite	Trr	Ca_5	$(AsO_4)_3$	Cl
16	Vanadinite	Vna	Pb_5	$(VO_4)_3$	Cl
	Hedyphane Group		**M**	**T**	**X**
17	Aiolosite	Aio	Na_4Bi	$(SO_4)_3$	Cl
18	Caracolite	Cco	Na_3Pb_2	$(SO_4)_3$	Cl
19	Cesanite	Csa	Na_3Ca_2	$(SO_4)_3$	(OH)
20	Fluorphosphohedyphane	Fphdy	Ca_2Pb_3	$(PO_4)_3$	F
21	Fluorsigaiite§	Fgst	Ca_2Sr_3	$(PO_4)_3$	F
22	Hedyphane	Hdp	Ca_2Pb_3	$(AsO_4)_3$	Cl
23	Hydroxylhedyphane	Hhdy	Ca_2Pb_3	$(PO_4)_3$	(OH)
24	Miyahisaite§	Miy	$(Sr,Ca)_2Ba_3$	$(PO_4)_3$	F
25	Morelandite	Mldt	Ca_2Ba_3	$(AsO_4)_3$	Cl
26	Phosphohedyphane	Phdy	Ca_2Pb_3	$(PO_4)_3$	Cl
27	Parafiniukite§	Pfn	Ca_2Mn_3	$(PO_4)_3$	Cl
28	Vanackerite§	Vnk	Pb_4Cd	$(AsO_4)_3$	Cl
	Belovite Group		**M**	**T**	**X**
29	Belovite-(Ce)	Blv-Ce	$NaCeSr_3$	$(PO_4)_3$	F
30	Belovite-(La)	Blv-La	$NaLaSr_3$	$(PO_4)_3$	F
31	Carlgieseckeite-(Nd) §	Csk-Nd	$NaNdSr_3$	$(PO_4)_3$	F
32	Deloneite	Dln	$(Na_{0.5}REE_{0.25}Ca_{0.25})(Ca_{0.75}REE_{0.25})Sr_{1.5}(CaNa_{0.25}REE_{0.25})$	$(PO_4)_3$	$F_{0.5}(OH)_{0.5}$

Table 1. ... Continued

Row	Belovite group	Symbol	M	T	X
33	Fluorcaphite	Fcp	$SrCaCa_3$	$(PO_4)_3$	F
34	Fluorstrophite	Fstr	$SrCaSr_3$	$(PO_4)_3$	F
35	Kuannersuite-(Ce)	Kua-Ce	$NaCeBa_3$	$(PO_4)_3$	$F_{0.5}Cl_{0.5}$
	Britholite Group		**M**	**T**	**X**
36	Britholite-(Ce)	Bri-Ce	$(Ce,Ca)_5$	$(SiO_4)_3$	(OH)
37	Britholite-(Y)	Bri-Y	$(Y,Ca)_5$	$(SiO_4)_3$	(OH)
38	Fluorbritholite-(Ce)	Fbri-Ce	$(Ce,Ca)_5$	$(SiO_4)_3$	F
39	Fluorbritholite-(Y)	Fbri-Y	$(Y,Ca)_5$	$(SiO_4)_3$	F
40	Fluorbritholite-(Nd) [§]	Fbri-Nd	Ca_2,Nd_3	$(SiO_4)_3$	F
41	Fluorcalciobritholite	Fcbri	$(Ca,REE)_5$	$(SiO_4,PO_4)_3$	F
42	Tritomite-(Ce)	Tto-Ce	Ca_5	$(SiO_4,BO_4)_3$	(OH,O)
43	Tritomite-(Y)	Tto-Y	Y_5	$(SiO_4,BO_4)_3$	(O,OH,F)
	Ellestadite Group		**M**	**T**	**X**
44	Chlorellestadite [§]	Clel	Ca_5	$(SiO_4)_{1.5}(SO_4)_{1.5}$	Cl
45	Fluorellestadite	Fel	Ca_5	$(SiO_4)_{1.5}(SO_4)_{1.5}$	F
46	Hydroxylellestadite	Hel	Ca_5	$(SiO_4)_{1.5}(SO_4)_{1.5}$	(OH)
47	Mattheddleite	Mhd	Pb_5	$(SiO_4)_{1.5}(SO_4)_{1.5}$	(Cl,OH)

Symbols from Warr (2021); § = Fluoralforsite (Krzątała et al., in press; row 3), Fluorpyromorphite (Kasatkin et al., 2023; row 5), Hydroxylpyromorphite (Olds et al., 2021; row 7), Pieczkaite (Tait et al., 2015; row 10), Pliniusite (Pekov et al., 2022; row 11), Fluorsigaiite (Wu et al., 2022; row 21), Miyahisaite (Nishio-Hamane et al., 2012; row 24), Parafiniukite (Pieczka et al., 2018; row 27), Vanackerite (Schlüter et al., 2016; row 28), Carlgieseckeite-(Nd) (Pekov et al., 2012; row 31), Fluorbritholite-(Nd) (Holstam et al., in press; row 40) and Chlorellestadite (Środek et al., 2018; row 44) are new apatite supergroup species approved by the IMA later than the subcommittee report by Pasero et al. (2010).

technique, without any direct determination of the H_2O (wt%) content: (a) Calculation and classification of apatite supergroup minerals on the basis of 13 total anions. In case of the analytical value for H_2O (wt%) is available, this procedure will not result in exactly 12 O and 1 (F+Cl+OH) with a total of 13 anions. Although the total amounts of O and (F+Cl+OH) not significantly different from these values, some O^{2-} may substitute for monovalent anions at the X site depending on the overall positive charges associated with cations. On the other hand, in case of the analytical value for H_2O (wt%) is lacking in the tabulated mineral analysis as in the EMPA data, it is reasonable to assume a calculated H_2O (wt%) so as to give 13 total anions (O+F+Cl+OH), with O=12 and (F+Cl+OH)=1. If [F+Cl (*apfu*)] ≥1, stoichiometric estimation of H_2O (wt%) content should be omitted (Pasero et al., 2010). (b) Calculation and classification of apatite supergroup minerals on the basis of 8 total cations

(i.e., ∑ M+T=8 (*apfu*)). (c) Calculation and classification of apatite supergroup minerals on the basis of 3T cations [i.e., ∑ P+As+V+Si+S=3 (*apfu*)].

According to Pasero et al. (2010), unless the structural vacancies are possible at some sites, in principle, criterion (a) is preferable to criteria (b) and (c). The allocation of cations such as P^{5+}, As^{5+}, V^{5+}, Si^{4+} and S^{6+} can be assumed to be in the tetrahedral coordination and, thus assigned to the T site. In cases of a significant deviation from an ideal sum of 3 (*apfu*), it is concluded that the analysis is incorrect, or unreliable due to the admixture of other phases or any other similar problems (Pasero et al., 2010). Following the allocation of cations at the T site, all remaining cations in the apatite supergroup analysis will enter the M1 and M2 sites. However, an explanation of partitioning between these two sites is not so easy without an accurate evaluation of the electron density at each of them that also requires a necessary structural study. Nevertheless,

Pasero et al., (2010) suggested that the allocation of M cations maybe arranged in order of their increasing ionic radius. For example, the M1 site is filled with smaller cations, particularly Ca, and the M2 site is allocated with larger cations such as Ba and Pb. Although this approach results in correct allocations of cations in most cases for identification or naming the apatite supergroup species, it is not also perfect as some doubts remain regarding cation partitioning trends in apatite, especially in the partitioning of Ca and REE contents between the M1 and M2. For example, parafiniukite $[Ca_2Mn_3(PO_4)_3Cl]$ with smaller Mn^{2+} at M2 and larger Ca at M1 does not follow the rule that cations fill at first M1 and then M2 in order of increasing ionic radii. In short, cations with charges of +4, +5 and +6 prefer to occupy the T site in the apatite supergroup structure and cations with charges of +1, +2 and +3 favour the M sites. Thus, the overall charge associated with anions is -25 [i.e., $12O^{2-}+1(F, Cl, OH)^-$]. In conclusion, considering the complexity of crystal chemistry, Pasero et al. (2010) proposed a procedure for the apatite supergroup nomenclature scheme: each combination of M1, M2, and T dominant cations should deserve a specific root name and adjectival prefixes for the X anions also be preferred over the modified Levinson suffixes due to the historical and practical reasons. In this regard, for example, it is not recommended to rename pyromorphite $[Pb_5(PO_4)_3Cl]$ as chlorpyromorphite, but F-dominant analogue of pyromorphite has been named fluorpyromorphite $[Pb_5(PO_4)_3F]$ by Kasatkin et al. (2023) as a new apatite group species. Similarly, OH-dominant analogue of pyromorphite was named as hydroxylpyromorphite $[Pb_5(PO_4)_3(OH)]$ by Olds et al. (2021).

PROGRAM DESCRIPTION

WinApclas is a user-friendly compiled program package ($\approx$17 Mb) for apatite supergroup mineral analyses developed for personal computers running in the Microsoft® Windows operating system. The program first calculates cations and anions (*apfu*) values from electron-microprobe and wet chemical apatite supergroup analyses and then classifies the currently valid 47 species that belong to the five groups including apatite, hedyphane, belovite, britholite and ellestadite (see Table 1). A list of the calculation steps in the *Calculation Screen* and in an Excel output of developed program is given in Table 2. Currently, two approaches (i.e., Piccoli and Candela, 2002; Ketcham, 2015) are available in estimation of the mole fractions of fluorapatite (X_F), chlorapatite (X_{Cl}) and hydroxylapatite (X_{OH}). Although the Ketcham (2015) improved calculation method allows EMPA analyses to be estimated more rigorously with a higher standard that removes errors of up to 4 % in stoichiometric calculations,

the method of Piccoli and Candela (2002) is used in estimation of the X_F, X_{Cl} and X_{OH} values considering apatite analyses from several studies only report the F and Cl contents.

Data entry of the apatite supergroup mineral analyses

Upon successful installation of WinApclas, the start-up screen with various pull-down menus and equivalent shortcuts appears on the screen (Figure 1a). The program allows the user to type wet chemical or electron-microprobe apatite supergroup mineral analyses (wt%), the whole-rock or melt SiO_2 and P_2O_5 (wt%) and trace and REE (ppm) contents of apatite by clicking the *New* icon on the tool bar, by selecting the *New File* from the pull-down menu of *File* option or pressing the *Ctrl + N* keys. In the *New File* or *Data Entry Screen*, these input parameters are highlighted by the soft green, pink and blue colours, respectively. The standard 54 variables (wt%) are used by WinApclas for calculation and classification of the apatite supergroup mineral analyses as in the following orders (Figure 1b):

Sample No [Apatite supergroup], SiO_2, TiO_2, ZrO_2, UO_2, ThO_2, SnO_2, CO_2, Al_2O_3, Cr_2O_3, V_2O_3, Sb_2O_3, Fe_2O_3, Mn_2O_3, B_2O_3, As_2O_3, Bi_2O_3, Y_2O_3, La_2O_3, Ce_2O_3, Pr_2O_3, Nd_2O_3, Sm_2O_3, Eu_2O_3, Gd_2O_3, Tb_2O_3, Dy_2O_3, Ho_2O_3, Er_2O_3, Tm_2O_3, Yb_2O_3, Lu_2O_3, P_2O_5, As_2O_5, V_2O_5, Nb_2O_5, SO_3, SeO_3, MgO, NiO, FeO, CoO, MnO, PbO, ZnO, CuO, CdO, BaO, CaO, SrO, Na_2O, K_2O, F, Cl and H_2O (wt%).

On the other hand, in the *New File* or *Data Entry Screen*, WinApclas provides the user to type whole-rock SiO_2 and P_2O_5 (wt%) contents for apatite saturation temperature (ºC) estimations to be displayed in the *Calculation Screen*. Similarly, REE (La to Lu) as well as some trace element (ppm) contents (i.e., Mn, Sr, Mg, Y, Pb, Th, U, Zr and V) can be typed in the *New File* or *Data Entry Screen*, to be used especially for discrimination plots (e.g., Mao et al., 2016; Rukhlov et al., 2016) of apatite compositions from porphyry and related ore deposits (e.g., porphyry Cu-Mo-Au, W skarn, iron oxide copper-gold, Au±Co, Cu, Pb-Zn skarns, etc.). However, if trace and REE (ppm) contents with blue colour labels are absent in the *Data Entry Screen* (i.e., La to V), but their oxide equivalents (i.e., La_2O_3 to V_2O_5) are available in the soft green labels then the program converts oxide compositions (wt%) to elements (ppm) and continues to display these plots with the help of Grapher program. Apatite supergroup analyses typed in an Excel file with the extension of ".xls" and ".xlsx" as in the above order can be loaded into the program's *Data Entry Screen* by clicking the *Open Excel File* option from the pull-down menu of *File*. By selecting the *Edit Excel File* option from the pull-down menu of *File*, these can be typed in a blank Excel file (i.e., MyApatite), stored

Table 2. Description of column numbers in the *Calculation Screen* window of WinApclas program and an output Excel file.

| Row	Explanations	Column Numbers
1	Major oxide apatite supergroup mineral analyses (wt%)	1-57
2	Blank	58
3	Calculated H_2O (wt%) content based on the stoichiometric constraints	59
4	Blank	60
5	Recalculated cations and anions of the apatite supergroup mineral analyses (*apfu*)	61-112
6	Blank	113
7	O, F, Cl and OH contents of the apatite supergroup mineral analyses (*apfu*)	114-117
8	Blank	118
9	Mole fractions of F, Cl and OH contents of the apatite supergroup mineral analyses (*apfu*)	119-122
10	Blank	123
11	Total M site content of the apatite supergroup mineral analyses (*apfu*)	124
12	Total T site content of the apatite supergroup mineral analyses (*apfu*)	125
13	Total (M+T) sites content of the apatite supergroup mineral analyses (*apfu*)	126
14	Ratio of the total M and T site (M/T) of the apatite supergroup mineral analyses	127
15	Blank	128
16	Total M site charge values of the apatite supergroup mineral analyses	129
17	Total T site charge values of the apatite supergroup mineral analyses	130
18	Total (M+T) sites charge values of the apatite supergroup mineral analyses	131
19	Blank	132
20	Total rare earth element (REE) contents of the apatite supergroup mineral analyses	133
21	(Ce/Ce*)$_N$ anomaly values of the apatite supergroup mineral analyses	134
22	(Eu/Eu*)$_N$ anomaly values of the apatite supergroup mineral analyses	135
23	Blank	136
24	Dominant M site components of the apatite supergroup mineral analysis	137
25	Dominant T site components of the apatite supergroup mineral analysis	138
26	Dominant X site components of the apatite supergroup mineral analysis	139
27	Blank	140
28	Group and species of the apatite supergroup mineral analyses	141-142
29	Blank	143
30	SiO_2 (wt%) contents of the whole-rock or melt analyses	144
31	P_2O_5 (wt%) contents of the whole-rock or melt analyses	145
32	P_2O_5 (wt%) contents of the apatite supergroup mineral analyses	146
33	Blank	147
34	Apatite saturation temperature (AST, ºC) values calculated by the Harrison and Watson (1984) model	148
35	Apatite saturation temperature (AST, ºC) values calculated by the Piccoli and Candela (2002) model	149
36	Average apatite saturation temperature (AST, ºC) values of two models	150
37	Blank	151
38	Oxygen fugacity (log fO_2) values calculated from apatite compositions using the model by Miles et al. (2014)	152
39	Calculated FMQ (i.e., Fayalite-Magnetite-Quartz) values using the model by Myers and Eugster (1983)	153
40	Calculated ΔFMQ values by combining the model by Miles et al. (2014) and Myers and Eugster (1983)	154
41	Blank	155
42	Calculated Cl contents (ppm) in the melt using the model by Mathez and Webster (2005)	156

Table 2. ... Continued

Row	Explanations	Column Numbers
43	Calculated F contents (ppm) in the melt using the model by Mathez and Webster (2005)	157
44	Calculated Cl contents (ppm) in the melt using the model by Li and Costa (2020)	158
45	Calculated F contents (ppm) in the melt using the model by Li and Costa (2020)	159
46	Calculated H_2O contents (wt%) in the melt from Cl using the model by Li and Costa (2020)	160
47	Calculated H_2O content (wt%) in the melt from F using the model by Li and Costa (2020)	161
48	Average H_2O contents (wt%) in the melt from Cl and F (i.e., calculated using the model by Li and Costa (2020)	162
49	Calculated S contents (ppm) in the melt using the model by Peng et al. (1997)	163
50	Calculated S contents (ppm) in the melt using the model by Parat et al. (2011)	164
51	Average S contents (ppm) in the melt (i.e., calculated by the models Peng et al. (1997) and Parat et al. (2011)	165
52	Blank	166
53	Calculated H_2O contents (wt%) based on apatite Cl compositions from porphyry-type deposits using the empirical correlation model by Huang et al. (2023)	167
54	Calculated H_2O contents (wt%) based on apatite F compositions from porphyry-type deposits using the empirical correlation model by Huang et al. (2023)	168
55	Calculated H_2O contents (wt%) based on apatite Cl/F ratios from porphyry-type deposits using the model by Huang et al. (2023)	169
56	Average H_2O contents (wt%) based on apatite Cl and F concentrations and Cl/F ratios from porphyry-type deposits (i.e., calculated from the model by Huang et al. 2023)	170
57	Calculated pressure (kbar) values based on apatite Cl compositions from porphyry-type deposits using the empirical correlation model by Huang et al. (2023)	171
58	Calculated pressure (kbar) values based on apatite F compositions from porphyry-type deposits using the empirical correlation model by Huang et al. (2023)	172
59	Calculated pressure (kbar) values based on apatite Cl/F ratios from porphyry-type deposits using the model by Huang et al. (2023)	173
60	Average pressure (kbar) values based on apatite Cl and F concentrations and Cl/F ratios from porphyry-type deposits (i.e., calculated from the model by Huang et al., 2023)	174
61	Calculated depth (km) values based on apatite Cl compositions from porphyry-type deposits using the empirical correlation model by Huang et al. (2023)	175
62	Calculated depth (km) values based on apatite F compositions from porphyry-type deposits using the empirical correlation model by Huang et al. (2023)	176
63	Calculated depth (km) values based on apatite Cl/F ratios from porphyry-type deposits using the model by Huang et al. (2023)	177
64	Average depth (km) values based on apatite Cl and F concentrations and Cl/F ratios from porphyry-type deposits (i.e., calculated from the model by Huang et al., 2023)	178
65	Blank	179

apfu = Atoms per formula unit; $(Ce/Ce^*)_N = \sqrt{La_N + Pr_N}$; $(Eu/Eu^*)_N = \sqrt{Sm_N + Sm_N}$; Chondrite composition values from Lodders (2010); AST = Apatite Saturation Temperature.

in a different file name with the extension of ".xls" or ".xlsx", and then loaded into the program's *Data Entry Screen* by clicking the *Open Excel File* option from the pull-down menu of *File*. Additional information about the data entry or similar topics can be accessed by pressing the F1 function key to display the WinApclas.chm file on

the screen. Current version of WinApclas presents total 48 binary and ternary classification and compositional plots. These plots are displayed by the Golden Software's Grapher program by selecting any diagram type from the pull-down menu of *Graph* in the *Calculation Screen* of program (Figure 1c).
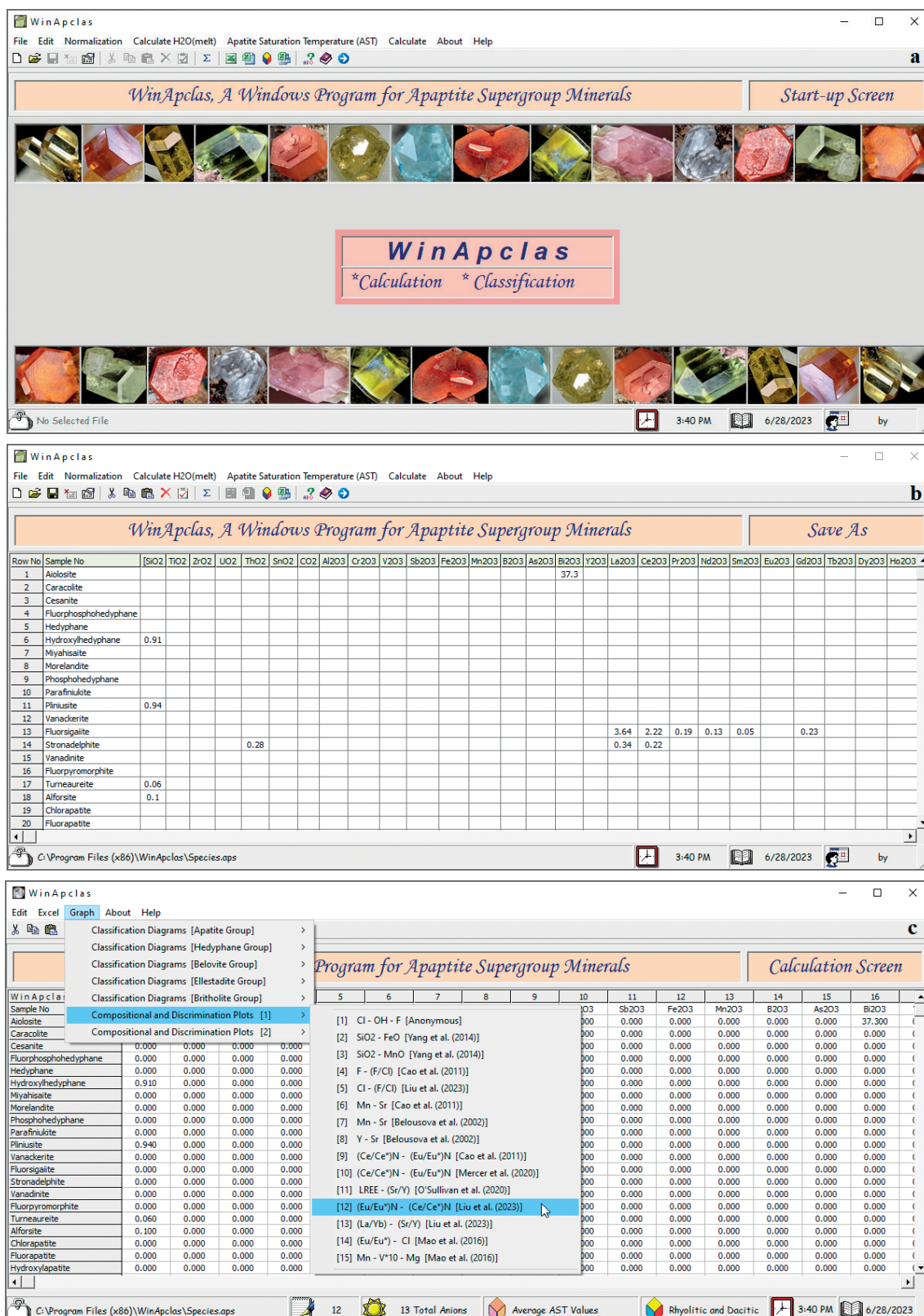
Figure 1. a) Screenshot of the WinApclas Start-up window with various pull-down menus and equivalent shortcuts; b) Screenshot of the WinApclas Data Entry window with the total of 79 input variables; c) Screenshots of selecting the binary and ternary compositional and discrimination plot diagram types in the Calculation Screen.

WORKED EXAMPLES

Due to the large compositional variability, apatite has been used as a good monitor: to constrain and reconstruct the source composition, to understand various magmatic processes including differentiation and fluid exsolution, to estimate crystallization temperature and redox conditions and to determine metasomatic processes (Teiber et al., 2015; see references therein). Using the selected data set from literature, the following examples show how WinApclas can be used in estimation and classification of the apatite supergroup minerals. Once the previously typed or loaded analyses are processed by clicking the *Calculate* icon (i.e. ∑) in the *Data Entry Section* of the program, all input and estimation parameters are displayed in columns 1-178 (see Table 2) of the *Calculation Screen*. Pressing the Ctrl+F keys or clicking the *Open File to Calculate* option from the *Calculate* menu also executes the data processing for a selected data file with the extension of ".aps". By clicking the *Send results to Excel file* icon in the *Calculation Screen*, all calculations can be stored in an Excel file (Output.xlsx) and then displayed by clicking the *Open and edit Excel file* icon. Validity of program outputs for classification of apatite supergroup species has been tested with representative mineral analyses (see Table 3, Table 4 and Table 5) selected from the literature (e.g., Dunn et al., 1980; Cavarretta et al., 1981; Anthony et al., 2001-2005; Chakhmouradian et al., 2005; Kampf et al., 2006; Pekov et al., 2010, 2011, 2012, 2022; Nishio-Hamane et al., 2012; Tait et al., 2015; Schlüter et al., 2016; Pieczka et al., 2018; Środek et al., 2018; Rakovan and Hughes, 2000; Olds et al., 2021; Wu et al., 2022; Kasatkin et al., 2023; Holtsam et al., 2023). Examples of classification and compositional and discrimination plots by WinApclas from the pull-down menu of *Graph* in the *Calculation Screen* are given in Figure 2 and Figure 3, respectively.

Calculation of apatite saturation temperature

Experimental studies on the crystallization of apatite in igneous systems (i.e., melt compositions from peralkaline to peraluminous and ultramafic to rhyolitic) showed that, in general, the solubility of apatite in melts increases with increasing temperature, with decreasing polymerization of the melts and also the decreasing silica content of melt (London et al., 1999). According to Harrison and Watson (1984), apatite crystallization is mainly controlled by the SiO_2 and P_2O_5 contents as well as the temperature in silicate melts with 45 to 75 wt% SiO_2 and 0 to 10 wt% water concentrations within the temperature range from 850 to 1500 °C at crustal pressure conditions. When compared to the other minerals, apatite saturates relatively at early stages over a wide temperature range in most felsic metaluminous magmatic system. Piccoli and Candela (2002) proposed a model to estimate the

apatite saturation temperature (AST) for metaluminous to slightly peraluminous systems using the Nernst partition coefficients presented by Harrison and Watson (1984). WinApclas estimates and lists the AST (°C) models of Harrison and Watson (1984) and Piccoli and Candela (2002) together with their average values for apatite analyses in the *Calculation Screen* (i.e., in columns 148 to 150), provided that the SiO_2 and P_2O_5 (wt%) contents of whole-rock or melt compositions with pink colour labels are available in the *Data Entry Screen*. The program considers the average AST (°C) value, as a default, in the temperature-dependent exchange equations (e.g., K_D $_{OH-Cl}^{Apatite-melt}$). At the same time, WinApclas provides the user to select the Harrison and Watson (1984) or Piccoli and Candela (2002) model options form the pull-down menu of *Apatite Saturation Temperature (AST)* in the *Data Entry Screen* for these types of calculations. Examples of the calculated AST (°C) values by program using the apatite compositions associated with whole-rock compositions from Du et al. (2022) are listed in Table 6 (see rows 34 to 36).

Estimation of redox state from apatite manganese composition

The oxidation states of magmas contribute important information about the metallogenic properties of plutonic rocks, their source rock compositions and tectonic settings and release and speciation of volatile elements during volcanic eruptions (Miles et al., 2014). For example, concentrations of redox sensitive elements (e.g., Fe, Mn, Ce and Eu) in several accessory minerals (e.g., Ce anomalies in zircon) provide valuable knowledge in obtaining the reliable estimates of redox states of magmas (e.g., Figure 3a). In this context, the Mn content as well as the Ce and Eu anomaly values in apatite compositions can be used to obtain the relative oxygen fugacity of the magmatic rocks in relation to the mineralization systems. Quantitative estimates of redox conditions can be obtained using the oxygen fugacity (fO_2) that means a measure of the availability and capacity of oxygen to participate in reactions between minerals and fluids. Miles et al. (2014) observed that the variation of Mn contents of apatite compositions in intermediate to silicic magmas can be used as a proxy for assessing the degree of oxidation. They investigated the use of Mn concentrations in coexisting apatite compositions to record changing redox conditions in the post-Caledonian Criffel granitic pluton, southern Scotland. However, Marks et al. (2016) suggested that a given Mn concentration in apatite may indicate either relatively reduced or quite oxidized conditions as in the case of syenitic rocks and leucogranites, respectively. Consequently, a common agreement on the Mills et al. (2014) model is that further empirical and experimental studies is required to fully investigate the potential of Mn-

Table 3. Chemical compositions of selected apatite group minerals with calculations and classifications by WinApclas.

Row		S1	S2	S3	S4	S5	S6	S7	S8	S9	S10	S11	S12
1	SiO_2	0.100	0.000	0.000	0.000	0.000	0.000	0.000	0.940	0.000	0.190	0.000	0.060
2	La_2O_3	0.000	0.000	0.000	0.000	0.000	0.000	0.000	0.000	0.340	0.000	0.000	0.000
3	Ce_2O_3	0.000	0.000	0.000	0.000	0.000	0.000	0.000	0.000	0.220	0.000	0.000	0.000
4	P_2O_5	22.700	41.200	15.900	15.770	1.700	0.140	37.520	5.630	29.020	0.210	0.300	0.200
5	As_2O_5	0.000	0.000	0.000	0.000	52.200	23.170	0.000	13.260	0.000	51.210	0.000	51.760
6	V_2O_5	0.000	0.000	0.000	0.000	0.000	0.000	0.000	27.040	0.000	0.040	19.100	0.010
7	SO_3	0.000	0.000	0.000	0.000	0.000	0.000	0.000	1.730	0.000	0.490	0.000	0.220
8	MgO	0.000	0.000	0.000	0.000	0.100	0.000	0.000	0.000	0.000	0.000	0.000	0.000
9	FeO	0.000	0.000	0.000	0.000	0.200	0.000	2.450	0.260	0.000	0.000	0.000	0.000
10	MnO	0.000	0.000	0.000	0.000	0.000	0.000	41.770	0.000	0.000	0.480	0.000	1.890
11	PbO	0.800	0.000	82.500	82.200	0.000	74.580	0.000	0.000	0.000	5.190	78.070	0.100
12	BaO	67.700	0.000	0.000	0.000	0.000	0.000	0.000	0.000	2.400	0.000	0.000	0.520
13	CaO	4.600	53.400	0.150	0.000	43.500	0.000	13.780	48.040	2.490	39.310	0.070	41.390
14	SrO	2.700	0.000	0.000	0.000	0.000	0.000	0.000	0.580	62.720	0.030	0.000	0.120
15	Na_2O	0.000	0.000	0.000	0.000	0.000	0.000	0.000	0.330	0.100	0.130	0.000	0.020
16	F	0.700	0.130	1.360	0.460	0.200	0.000	0.000	3.460	1.450	2.120	0.000	0.320
17	Cl	3.600	6.200	0.000	0.150	0.100	2.390	3.860	0.000	0.000	0.080	2.660	2.560
18	O=F	0.295	0.055	0.573	0.194	0.084	0.000	0.000	1.457	0.611	0.893	0.000	0.135
19	O=Cl	0.812	1.399	0.000	0.034	0.023	0.539	0.871	0.000	0.000	0.018	0.600	0.578
20	H_2O	0.000	0.090	0.000	0.460	1.300	0.000	0.600	0.000	0.540	0.330	0.000	0.580
21	$\sum$ (wt%)	101.793	99.566	99.337	98.812	99.193	99.741	99.109	99.823	98.949	98.899	99.600	99.038
22	$H_2O_{calculated}$	0.000	0.000	0.013	0.000	0.000	0.000	0.000	0.000	0.000	0.000	0.000	0.000
23	Si	0.015	0.000	0.000	0.000	0.000	0.000	0.000	0.089	0.000	0.021	0.000	0.007
24	La	0.000	0.000	0.000	0.000	0.000	0.000	0.000	0.000	0.016	0.000	0.000	0.000
25	Ce	0.000	0.000	0.000	0.000	0.000	0.000	0.000	0.000	0.010	0.000	0.000	0.000
26	P	2.917	3.025	3.008	3.080	0.157	0.029	3.062	0.451	3.064	0.020	0.059	0.019
27	As^{5+}	0.000	0.000	0.000	0.000	2.978	2.989	0.000	0.655	0.000	2.990	0.000	2.990
28	V^{5+}	0.000	0.000	0.000	0.000	0.000	0.000	0.000	1.689	0.000	0.003	2.954	0.001
29	S	0.000	0.000	0.000	0.000	0.000	0.000	0.000	0.123	0.000	0.041	0.000	0.018
30	Mg	0.000	0.000	0.000	0.000	0.016	0.000	0.000	0.000	0.000	0.000	0.000	0.000
31	Fe^{2+}	0.000	0.000	0.000	0.000	0.018	0.000	0.197	0.021	0.000	0.000	0.000	0.000
32	Mn	0.000	0.000	0.000	0.000	0.000	0.000	3.410	0.000	0.000	0.045	0.000	0.177
33	Pb	0.033	0.000	4.963	5.104	0.000	4.954	0.000	0.000	0.000	0.156	4.920	0.003
34	Ba	4.027	0.000	0.000	0.000	0.000	0.000	0.000	0.000	0.117	0.000	0.000	0.023
35	Ca	0.748	4.963	0.036	0.000	5.085	0.000	1.423	4.866	0.333	4.703	0.018	4.900
36	Sr	0.238	0.000	0.000	0.000	0.000	0.000	0.000	0.032	4.536	0.002	0.000	0.008
37	Na	0.000	0.000	0.000	0.000	0.000	0.000	0.000	0.060	0.024	0.028	0.000	0.004
38	$\sum$ (apfu)	7.978	7.988	8.007	8.184	8.254	7.973	8.092	7.987	8.109	8.010	7.952	8.149

Table 3. ... Continued

Row		S1	S2	S3	S4	S5	S6	S7	S8	S9	S10	S11	S12
39	F	0.336	0.036	0.961	0.336	0.069	0.000	0.000	1.034	0.572	0.749	0.000	0.112
40	Cl	0.926	0.911	0.000	0.059	0.018	0.999	0.631	0.000	0.000	0.015	1.055	0.479
41	OH	0.000	0.027	0.039	0.473	0.844	0.001	0.234	0.000	0.282	0.139	0.000	0.266
42	X_F	0.266	0.037	0.961	0.449	0.123	0.000	0.000	1.000	0.718	0.844	0.000	0.139
43	X_{Cl}	0.734	0.937	0.000	0.078	0.033	0.999	0.766	0.000	0.000	0.017	1.000	0.596
44	X_{OH}	0.000	0.027	0.039	0.473	0.844	0.001	0.234	0.000	0.282	0.139	0.000	0.266
45	$\sum (apfu)$	1.000	1.000	1.000	1.000	1.000	1.000	1.000	1.000	1.000	1.000	1.000	1.000
46	$\sum$ M site $(apfu)$	5.046	4.963	4.999	5.104	5.120	4.954	5.031	4.980	5.036	4.935	4.938	5.114
47	$\sum$ T site $(apfu)$	2.932	3.025	3.008	3.080	3.135	3.018	3.062	3.007	3.072	3.075	3.014	3.034
48	$\sum$ M/$\sum$ T	1.721	1.640	1.662	1.657	1.633	1.641	1.643	1.656	1.639	1.605	1.638	1.685
49	Dominant M site	Ba_5	Ca_5	Pb_5	Pb_5	Ca_5	Pb_5	Mn_5	Ca_5	Sr_5	Ca_5	Pb_5	Ca_5
50	Dominant T site	$(PO_4)_3$	$(PO_4)_3$	$(PO_4)_3$	$(PO_4)_3$	$(AsO_4)_3$	$(AsO_4)_3$	$(PO_4)_3$	$(VO_4)_3$	$(PO_4)_3$	$(AsO_4)_3$	$(VO_4)_3$	$(AsO_4)_3$
51	Dominant X site	Cl	Cl	F	OH	OH	Cl	Cl	F	F	F	Cl	Cl
52	Group name	ApG	ApG	ApG	ApG	ApG	ApG	ApG	ApG	ApG	ApG	ApG	ApG
53	Species	Afr	Clap	Fpym	Hpm	Jbm	Mim	Pzk	Pli	Sad	Sva	Vna	Trr

Samples of S1, S2, S6, S10, S11 and S12 = from Handbook of Mineralogy (Anthony et al., 2001-2005), S3 = from Kasatkin et al. (2023), S4 = from Olds et al. (2021), S5 = from Dunn et al. (1980), S7 = from Tait et al. (2015), S8 = from Pekov et al. (2022), S9 = from Pekov et al. (2010); The formulae were recalculated to 13 total anions; *apfu* = Atoms per formula unit; X_F, X_{Cl} and X_{OH} = Mole fractions of F, Cl and OH, respectively; ApG = Apatite group; Afr = Alforsite, Clap = Chlorapatite, Fpym = Fluorpyromorphite, Hpm = Hydroxylpyromorphite, Jbm = Johnbaumite, Mim = Mimetite, Pzk = Pieczkaite, Pli = Pliniusite, Sad = Stronadelphite, Sva = Svabite, Vna = Vanadinite, Trr = Turneaureite.

in-apatite oxybarometer as a redox proxy (Miles et al., 2016).

The fayalite-magnetite-quartz buffer (FMQ) is the most commonly used oxygen buffer in petrological studies due to the majority of igneous rocks have equilibrated within a few log fO$_2$ units around these conditions (Frost, 1991). Since the FMQ is influenced at a minimum by pressure (e.g., Kress and Carmichael, 1991), the relative oxygen fugacity (i.e., ΔFMQ) is also calculated as a reference in geochemical and petrological investigations. WinApclas calculates and lists the log oxygen fugacity (fO$_2$), the fayalite-magnetite-quartz buffer (FMQ) and the relative oxygen fugacity (ΔFMQ) values (see rows 37 to 39 in Table 6) for apatite analysis in the *Calculation Screen* (i.e., in columns 152 to 154), if MnO (wt%) content of apatite composition is available in the *Data Entry Screen*.

Fluorine, chlorine, water and sulphur contents of melt using apatite composition

Volatiles are carried by magmas in different ways such as major components of fluid phases, as dissolved species in silicate melt or as constituents within the mineral structures. As silicate melts suffer degassing during ascent and also the released fluid phases are difficult to measure, it seems that the determination of the compositions of melt inclusions as well as the volatile-bearing minerals (e.g., mica, amphibole etc.) are the unique ways to understand the volatile concentrations in magmas which are emplaced at depths of crust (Parat et al., 2011). Thus, in controlling the eruptive styles of volcanoes, the compositions as well as the amounts of volatiles in subvolcanic melts play an important role for tracing the evolution of halogen and sulfur contents in magmatic system. However, it is difficult to determine directly these parameters because of the large number of variables such as volatile loss during magma transport to the surface and eruption processes. Melt inclusions in mineral structures can be used for these purposes, but samples under examination from volcanic and plutonic rocks may not contain suitable inclusions or they can be modified by a range of post-entrapment and re-equilibration processes giving rise to possible under- or over-estimation of the volatile contents (Parat et al.,

Table 4. Chemical compositions of selected hedyphane group minerals with calculations and classifications by WinApclas.

Row		S1	S2	S3	S4	S5	S6	S7	S8	S9	S10	S11	S12
1	SiO_2	0.000	0.000	0.000	0.000	0.000	0.000	0.000	0.000	0.000	0.000	0.000	0.910
2	Bi_2O_3	0.000	0.000	0.000	0.000	0.000	37.300	0.000	0.000	0.000	0.000	0.000	0.000
3	La_2O_3	0.000	0.000	0.000	0.000	0.000	0.000	0.000	0.000	0.000	3.640	0.000	0.000
4	Ce_2O_3	0.000	0.000	0.000	0.000	0.000	0.000	0.000	0.000	0.000	2.220	0.000	0.000
5	Pr_2O_3	0.000	0.000	0.000	0.000	0.000	0.000	0.000	0.000	0.000	0.190	0.000	0.000
6	Nd_2O_3	0.000	0.000	0.000	0.000	0.000	0.000	0.000	0.000	0.000	0.130	0.000	0.000
7	Sm_2O_3	0.000	0.000	0.000	0.000	0.000	0.000	0.000	0.000	0.000	0.050	0.000	0.000
8	Gd_2O_3	0.000	0.000	0.000	0.000	0.000	0.000	0.000	0.000	0.000	0.230	0.000	0.000
9	P_2O_5	39.200	24.850	2.050	18.400	0.000	0.000	0.000	0.000	22.880	31.870	0.400	0.960
10	As_2O_5	0.000	0.000	28.110	2.730	23.590	0.000	0.000	0.000	0.000	0.000	28.200	25.360
11	V_2O_5	0.000	0.000	0.000	0.000	0.000	0.000	0.000	0.000	0.000	0.000	0.000	0.070
12	SO_3	0.000	0.000	0.000	0.000	0.000	38.340	29.760	52.600	0.000	0.000	0.000	0.000
13	FeO	2.950	0.000	0.410	0.000	0.000	0.000	0.000	0.000	0.000	0.000	0.000	0.000
14	MnO	31.190	0.000	0.390	0.000	0.000	0.000	0.000	0.000	0.000	0.000	0.000	0.030
15	PbO	0.000	0.000	24.850	67.600	64.440	0.000	55.320	0.000	61.690	0.000	58.000	59.810
16	CdO	0.000	0.000	0.000	0.000	8.820	0.000	0.000	0.000	0.000	0.000	0.000	0.000
17	BaO	0.000	52.050	33.000	0.000	0.000	0.000	0.000	0.000	0.000	0.000	0.100	2.950
18	CaO	24.140	4.690	8.850	9.240	0.000	0.000	0.000	18.900	13.430	15.170	10.300	7.740
19	SrO	0.000	16.510	0.000	0.000	0.000	0.000	0.000	0.720	0.000	44.440	1.000	0.000
20	Na_2O	0.050	0.000	0.000	0.000	0.000	19.850	11.520	23.300	0.000	0.750	0.000	0.090
21	K_2O	0.000	0.000	0.000	0.000	0.000	0.000	0.000	0.210	0.000	0.000	0.000	0.000
22	F	0.390	1.990	0.000	0.000	0.000	0.000	0.000	0.250	2.190	1.910	0.000	0.060
23	Cl	3.130	0.060	3.690	3.320	1.510	5.680	4.390	0.440	0.000	0.000	3.300	1.030
24	O=F	0.164	0.838	0.000	0.000	0.000	0.000	0.000	0.105	0.922	0.804	0.000	0.025
25	O=Cl	0.706	0.014	0.833	0.749	0.341	1.282	0.991	0.099	0.000	0.000	0.745	0.232
26	H_2O	0.680	0.090	0.000	0.000	0.000	0.000	0.000	2.910	0.000	0.460	0.000	0.000
27	$\sum$ (wt%)	101.050	99.389	100.517	100.541	98.019	99.888	99.999	99.125	99.268	100.256	100.555	98.752
28	$H_2O_{calculated}$	0.000	0.000	0.000	0.002	0.117	0.000	0.000	0.000	0.000	0.000	0.000	0.445
29	Si	0.000	0.000	0.000	0.000	0.000	0.000	0.000	0.000	0.000	0.000	0.000	0.186
30	Bi	0.000	0.000	0.000	0.000	0.000	1.002	0.000	0.000	0.000	0.000	0.000	0.000
31	La	0.000	0.000	0.000	0.000	0.000	0.000	0.000	0.000	0.000	0.149	0.000	0.000
32	Ce	0.000	0.000	0.000	0.000	0.000	0.000	0.000	0.000	0.000	0.090	0.000	0.000
33	Pr	0.000	0.000	0.000	0.000	0.000	0.000	0.000	0.000	0.000	0.008	0.000	0.000
34	Nd	0.000	0.000	0.000	0.000	0.000	0.000	0.000	0.000	0.000	0.005	0.000	0.000
35	Sm	0.000	0.000	0.000	0.000	0.000	0.000	0.000	0.000	0.000	0.002	0.000	0.000
36	Gd	0.000	0.000	0.000	0.000	0.000	0.000	0.000	0.000	0.000	0.008	0.000	0.000
37	P	3.053	3.012	0.305	2.758	0.000	0.000	0.000	0.000	3.038	3.004	0.065	0.166
38	As^{5+}	0.000	0.000	2.582	0.253	2.992	0.000	0.000	0.000	0.000	0.000	2.828	2.704

Table 4. ... Continued

Row		S1	S2	S3	S4	S5	S6	S7	S8	S9	S10	S11	S12
39	V^{5+}	0.000	0.000	0.000	0.000	0.000	0.000	0.000	0.000	0.000	0.000	0.000	0.009
40	S	0.000	0.000	0.000	0.000	0.000	2.997	3.000	3.156	0.000	0.000	0.000	0.000
41	Fe^{2+}	0.227	0.000	0.060	0.000	0.000	0.000	0.000	0.000	0.000	0.000	0.000	0.000
42	Mn	0.000	0.000	0.000	0.000	0.000	0.000	0.000	0.000	0.000	0.000	0.000	0.000
43	Pb	2.430	0.000	0.058	0.000	0.000	0.000	0.000	0.000	0.000	0.000	0.000	0.005
44	Cd	0.000	0.000	1.175	3.222	4.208	0.000	2.000	0.000	2.605	0.000	2.995	3.284
45	Ba	0.000	2.921	2.272	0.000	0.000	0.000	0.000	0.000	0.000	0.000	0.008	0.236
46	Ca	2.379	0.720	1.666	1.753	0.000	0.000	0.000	1.619	2.257	1.810	2.117	1.691
47	Sr	0.000	1.371	0.000	0.000	0.000	0.000	0.000	0.033	0.000	2.869	0.111	0.000
48	Na	0.009	0.000	0.000	0.000	0.000	4.009	3.000	3.612	0.000	0.162	0.000	0.036
49	K	0.000	0.000	0.000	0.000	0.000	0.000	0.000	0.021	0.000	0.000	0.000	0.000
50	$\sum$ (*apfu*)	8.124	8.023	8.120	7.986	8.201	8.008	8.001	8.443	7.900	8.107	8.124	8.316
51	F	0.113	0.901	0.000	0.000	0.000	0.000	0.000	0.063	1.086	0.673	0.000	0.039
52	Cl	0.488	0.015	1.099	0.996	0.621	1.003	0.999	0.060	0.000	0.000	1.073	0.356
53	OH	0.258	0.045	0.000	0.004	0.379	0.000	0.001	0.863	0.000	0.203	0.000	0.605
54	X_F	0.140	0.940	0.000	0.000	0.000	0.000	0.000	0.070	1.000	0.797	0.000	0.039
55	X_{Cl}	0.602	0.015	1.000	0.996	0.621	1.000	0.999	0.066	0.000	0.000	1.000	0.356
56	X_{OH}	0.258	0.045	0.000	0.004	0.379	0.000	0.001	0.863	0.000	0.203	0.000	0.605
57	$\sum$ (*apfu*)	1.000	1.000	1.000	1.000	1.000	1.000	1.000	1.000	1.000	1.000	1.000	1.000
58	$\sum$ M site (*apfu*)	5.072	5.011	5.232	4.975	5.209	5.011	5.001	5.286	4.862	5.104	5.231	5.251
59	$\sum$ T site (*apfu*)	3.053	3.012	2.887	3.011	2.992	2.997	3.000	3.156	3.038	3.004	2.893	3.065
60	$\sum$ M/$\sum$ T	1.661	1.663	1.812	1.652	1.741	1.672	1.667	1.675	1.600	1.699	1.808	1.713
61	Dominant M site	Ca_2Mn_3	$(Sr,Ca)_2Ba_3$	Ca_2Ba_3	Ca_2Pb_3	Pb_4Cd	Na_4Bi	Na_3Pb_2	Na_3Ca_2	Ca_2Pb_3	Ca_2Sr_3	Ca_2Pb_3	Ca_2Pb_3
62	Dominant T site	$(PO_4)_3$	$(PO_4)_3$	$(AsO_4)_3$	$(PO_4)_3$	$(AsO_4)_3$	$(SO_4)_3$	$(SO_4)_3$	$(SO_4)_3$	$(PO_4)_3$	$(PO_4)_3$	$(AsO_4)_3$	$(AsO_4)_3$
63	Dominant X site	Cl	F	Cl	Cl	Cl	Cl	Cl	OH	F	F	Cl	OH
64	Group name	HdpG	HdpG	HdpG	HdpG	HdpG	HdpG	HdpG	HdpG	HdpG	HdpG	HdpG	HdpG
65	Species	Pfn	Miy	Mldt	Phdy	Vnk	Aio	Cco	Csa	Fphdy	Fgst	Hdp	Hhdy

Samples of S1 = from Pieczka et al. (2018), S2 = from Nishio-Hamane et al. (2012), S3, S6, S7, S9 and S11 = from Handbook of Mineralogy (Anthony et al., 2001–2005), S4 = from Kampf et al. (2006), S5 = from Schlüter et al. (2016), S8 = from Cavarretta et al. (1981), S10 = from Wu et al. (2022); The formulae were recalculated to 13 total anions; *apfu* = Atoms per formula unit; X_F, X_{Cl} and X_{OH} = Mole fractions of F, Cl and OH, respectively; HdpG = Hedyphane group; Pfn = Parafiniukite, Miy = Miyahisaite, Mldt = Morelandite, Phdy = Phosphohedyphane, Vnk = Vanackerite, Aio = Aiolosite, Cco = Caracolite, Csa = Cesanite, Fphdy = Fluorphosphohedyphane, Fgst = Fluorsigaiite, Hdp = Hedyphane, Hhdy = Hydroxylhedyphane.

2011; Li and Costa, 2020). The prevalence of apatite in most magmatic systems provides the best mineral for earth scientists to use it as a geologic tool to record the petrogenetic histories of rocks. Consequently, the presence of volatiles such as halogens, S, H_2O and CO_2 within its crystal structure has subjected to many studies (e.g., Figure 3b) for apatite composition in understanding the volatile contents of magmas and magmatic source

PM

Table 5. Chemical compositions of selected belovite, britholite and ellestadite group minerals with calculations and classifications by WinApclas.

Row		S1	S2	S3	S4	S5	S6	S7	S8	S9	S10	S11
1	SiO_2	0.900	0.240	0.560	0.570	0.500	20.890	22.700	21.030	17.670	15.300	7.650
2	UO_2	0.000	0.000	0.000	0.000	0.000	1.470	0.000	0.000	0.000	0.000	0.000
3	ThO_2	0.000	0.430	0.000	0.000	0.300	20.730	0.510	0.000	0.000	0.000	0.000
4	CO_2	0.000	0.000	0.000	0.000	0.000	0.000	0.100	0.000	0.000	0.660	0.000
5	Al_2O_3	0.000	0.000	0.000	0.000	0.000	0.000	0.750	0.000	0.000	1.840	0.000
6	Fe_2O_3	0.000	0.000	0.000	0.000	0.000	0.000	1.440	0.000	0.000	0.110	0.000
7	B_2O_3	0.000	0.000	0.000	0.000	0.000	0.000	0.000	0.000	0.000	0.000	0.000
8	Y_2O_3	0.000	0.010	0.000	0.000	0.000	0.000	46.910	7.010	0.000	0.000	0.000
9	La_2O_3	6.670	13.080	1.320	2.610	2.400	7.350	5.760	3.230	0.000	0.000	0.000
10	Ce_2O_3	12.470	8.150	10.600	4.780	9.600	18.610	4.470	16.350	0.000	0.000	0.000
11	Pr_2O_3	0.000	0.300	2.620	0.340	0.120	1.640	0.000	3.310	0.000	0.000	0.000
12	Nd_2O_3	3.740	0.300	15.080	1.480	4.300	5.100	0.000	19.510	0.000	0.000	0.000
13	Sm_2O_3	0.000	0.030	2.890	0.140	0.500	0.000	0.000	6.340	0.000	0.000	0.000
14	Gd_2O_3	0.000	0.010	0.520	0.000	0.000	0.000	0.000	4.950	0.000	0.000	0.000
15	Tb_2O_3	0.000	0.000	0.000	0.000	0.000	0.000	0.000	0.560	0.000	0.000	0.000
16	Dy_2O_3	0.000	0.000	0.000	0.000	0.000	0.000	0.000	2.520	0.000	0.000	0.000
17	Ho_2O_3	0.000	0.000	0.000	0.000	0.000	0.000	0.000	0.320	0.000	0.000	0.000
18	Er_2O_3	0.000	0.000	0.000	0.000	0.000	0.000	0.000	0.670	0.000	0.000	0.000
19	Tm_2O_3	0.000	0.000	0.000	0.000	0.000	0.000	0.000	0.070	0.000	0.000	0.000
20	Yb_2O_3	0.000	0.000	0.000	0.000	0.000	0.000	0.000	0.310	0.000	0.000	0.000
21	Lu_2O_3	0.000	0.000	0.000	0.000	0.000	0.000	0.000	0.030	0.000	0.000	0.000
22	P_2O_5	27.500	28.300	32.720	36.230	25.100	4.300	1.730	0.680	0.440	1.310	0.000
23	As_2O_5	0.000	0.000	0.000	0.000	0.000	0.000	0.000	0.080	0.000	0.000	0.000
24	SO_3	0.000	0.030	0.000	0.000	0.040	0.000	0.000	0.000	22.720	20.750	6.000
25	MgO	0.000	0.000	0.000	0.000	0.000	0.000	0.100	0.000	0.000	1.380	0.000
26	FeO	0.000	0.000	0.000	0.000	0.000	0.000	0.790	0.000	0.000	0.000	0.000
27	MnO	0.000	0.000	0.000	0.000	0.000	0.000	3.670	0.000	0.000	0.180	0.000
28	PbO	0.000	0.000	0.000	0.000	0.000	0.000	0.000	0.000	0.000	0.000	83.600
29	BaO	2.150	2.350	0.140	0.030	50.600	0.000	0.000	0.000	0.000	0.000	0.000
30	CaO	0.610	0.500	18.530	30.460	0.030	19.920	9.580	10.860	54.430	55.000	0.000
31	SrO	38.100	40.090	7.550	20.780	0.900	0.000	0.000	0.000	0.000	0.000	0.000
32	Na_2O	4.190	4.090	5.680	1.740	3.900	0.000	0.000	0.000	0.070	0.330	0.000
33	K_2O	0.000	0.000	0.000	0.000	0.090	0.000	0.000	0.000	0.000	0.100	0.000
34	F	2.390	2.040	2.800	2.170	1.900	0.000	0.500	0.600	0.400	3.600	0.000
35	Cl	0.030	0.000	0.060	0.000	1.200	0.000	0.000	0.420	4.230	0.000	2.400
36	O=F	1.006	0.859	1.179	0.914	0.800	0.000	0.211	0.253	0.168	1.516	0.000
37	O=Cl	0.007	0.000	0.014	0.000	0.271	0.000	0.000	0.095	0.954	0.000	0.542
38	H_2O	0.110	0.220	0.000	0.520	0.000	0.000	0.680	0.150	0.520	0.300	0.000
39	$\sum$ (wt%)	97.847	99.311	99.877	100.936	100.409	100.010	99.479	98.653	99.357	99.344	99.108
40	$H_2O_{calculated}$	0.000	0.000	0.069	0.000	0.000	0.000	0.000	0.000	0.000	0.000	0.003
41	Si	0.113	0.030	0.059	0.056	0.071	2.710	2.669	2.938	1.531	1.304	1.864
42	U	0.000	0.000	0.000	0.000	0.000	0.042	0.000	0.000	0.000	0.000	0.000
43	Th	0.000	0.012	0.000	0.000	0.010	0.612	0.014	0.000	0.000	0.000	0.000
44	C	0.000	0.000	0.000	0.000	0.000	0.000	0.016	0.000	0.000	0.077	0.000
45	Al	0.000	0.000	0.000	0.000	0.000	0.000	0.104	0.000	0.000	0.185	0.000
46	Fe^{3+}	0.000	0.000	0.000	0.000	0.000	0.000	0.127	0.000	0.000	0.007	0.000
47	B	0.000	0.000	0.000	0.000	0.000	0.000	0.000	0.000	0.000	0.000	0.000

Table 5. ... Continued

Row		S1	S2	S3	S4	S5	S6	S7	S8	S9	S10	S11
48	Y	0.000	0.001	0.000	0.000	0.000	0.000	2.935	0.521	0.000	0.000	0.000
49	La	0.308	0.600	0.052	0.094	0.125	0.352	0.250	0.166	0.000	0.000	0.000
50	Ce	0.571	0.371	0.412	0.171	0.498	0.884	0.192	0.836	0.000	0.000	0.000
51	Pr	0.000	0.014	0.101	0.012	0.006	0.078	0.000	0.168	0.000	0.000	0.000
52	Nd	0.167	0.013	0.572	0.052	0.217	0.236	0.000	0.973	0.000	0.000	0.000
53	Sm	0.000	0.001	0.106	0.005	0.024	0.000	0.000	0.305	0.000	0.000	0.000
54	Gd	0.000	0.000	0.018	0.000	0.000	0.000	0.000	0.229	0.000	0.000	0.00
55	Tb	0.000	0.000	0.000	0.000	0.000	0.000	0.000	0.026	0.000	0.000	0.000
56	Dy	0.000	0.000	0.000	0.000	0.000	0.000	0.000	0.113	0.000	0.000	0.000
57	Ho	0.000	0.000	0.000	0.000	0.000	0.000	0.000	0.014	0.000	0.000	0.000
58	Er	0.000	0.000	0.000	0.000	0.000	0.000	0.000	0.029	0.000	0.000	0.000
59	Tm	0.000	0.000	0.000	0.000	0.000	0.000	0.000	0.001	0.000	0.000	0.000
60	Yb	0.000	0.000	0.000	0.000	0.000	0.000	0.000	0.013	0.000	0.000	0.000
61	Lu	0.000	0.000	0.000	0.000	0.000	0.000	0.000	0.001	0.000	0.000	0.000
62	P	2.910	2.978	2.941	3.004	3.009	0.472	0.172	0.080	0.032	0.095	0.000
63	As^{5+}	0.000	0.000	0.000	0.000	0.000	0.000	0.000	0.006	0.000	0.000	0.000
64	S	0.000	0.003	0.000	0.000	0.004	0.000	0.000	0.000	1.477	1.328	1.097
65	Mg	0.000	0.000	0.000	0.000	0.000	0.000	0.018	0.000	0.000	0.175	0.000
66	Fe^{2+}	0.000	0.000	0.000	0.000	0.000	0.000	0.078	0.000	0.000	0.000	0.000
67	Mn	0.000	0.000	0.000	0.000	0.000	0.000	0.365	0.000	0.000	0.013	0.000
68	Pb	0.000	0.000	0.000	0.000	0.000	0.000	0.000	0.000	0.000	0.000	5.484
69	Ba	0.105	0.114	0.006	0.001	2.807	0.000	0.000	0.000	0.000	0.000	0.000
70	Ca	0.082	0.067	2.108	3.196	0.005	2.768	1.207	1.626	5.053	5.024	0.000
71	Sr	2.762	2.889	0.465	1.180	0.074	0.000	0.000	0.000	0.000	0.000	0.000
72	Na	1.015	0.986	1.169	0.330	1.071	0.000	0.000	0.000	0.012	0.055	0.000
73	K	0.000	0.000	0.000	0.000	0.016	0.000	0.000	0.000	0.000	0.011	0.000
74	$\sum (apfu)$	8.032	8.078	8.008	8.101	7.937	8.153	8.146	8.048	8.106	8.273	8.446
75	F	0.945	0.802	0.940	0.672	0.851	0.000	0.186	0.265	0.110	0.971	0.000
76	Cl	0.006	0.000	0.011	0.000	0.288	0.000	0.000	0.099	0.621	0.000	0.991
77	OH	0.046	0.102	0.049	0.202	0.000	1.000	0.589	0.161	0.171	0.081	0.009
78	X_F	0.948	0.898	0.940	0.798	0.747	0.000	0.411	0.610	0.124	0.919	0.000
79	X_{Cl}	0.006	0.000	0.011	0.000	0.253	0.000	0.000	0.229	0.705	0.000	0.991
80	X_{OH}	0.046	0.102	0.049	0.202	0.000	1.000	0.589	0.161	0.171	0.081	0.009
81	$\sum (apfu)$	1.000	1.000	1.000	1.000	1.000	1.000	1.000	1.000	1.000	1.000	1.000
82	$\sum$ M site $(apfu)$	5.009	5.055	5.008	5.042	4.844	4.317	5.276	5.024	5.065	5.470	5.484
83	$\sum$ T site $(apfu)$	3.023	3.022	3.000	3.059	3.093	3.836	2.871	3.024	3.041	2.803	2.961
84	$\sum$ M/$\sum$ T	1.657	1.673	1.669	1.648	1.566	1.126	1.838	1.661	1.666	1.951	1.852
85	Dominant M site	$NaCeSr_3$	$NaLaSr_3$	$NaNdCa_3$	$SrCaCa_3$	$NaCeBa_3$	$(Ce,Ca)_5$	$(Y,Ca)_5$	$(Nd,Ca)_5$	Ca_5	Ca_5	Pb_5
86	Dominant T site	$(PO_4)_3$	$(PO_4)_3$	$(PO_4)_3$	$(PO_4)_3$	$(PO_4)_3$	$(SiO_4)_3$	$(SiO_4)_3$	$(SiO_4)_3$	$(SiO_4)_{1.5}(SO_4)_{1.5}$	$(SiO_4)_{1.5}(SO_4)_{1.5}$	$(SiO_4)_{1.5}(SO_4)_{1.5}$
87	Dominant X site	F	F	F	F	$F_{0.5}Cl_{0.5}$	OH	OH	F	Cl	F	Cl,OH
88	Group name	BlvG	BlvG	BlvG	BlvG	BlvG	BriG	BriG	BriG	ElG	ElG	ElG
89	Species	Blv-Ce	Blv-La	Csk-Nd	Fcp	Kua-Ce	Bri-Ce	Bri-Y	Fbri-Nd	Clel	Fel	Mhd

Samples of S1 = from Rakovan and Huges (2000), S2, S5, S6, S7, S10 and S11 = from Handbook of Mineralogy (Anthony et al., 2001-2005), S3 = from Pekov et al. (2012), S4 = from Chakhmouradian et al. (2005), S8 = from Holtsam et al. (2023), S9 = from Środek et al. (2018); The formulae were recalculated to 13 total anions; *apfu* = Atoms per formula unit; X_F, X_{Cl} and X_{OH} = Mole fractions of F, Cl and OH, respectively; BlvG = Belovite group, BriG = Britholite group, ElG = Ellestadite group; Blv-Ce = Belovite-(Ce), Blv-La = Belovite-(La), Csk-Nd = Carlgieseckeite-(Nd), Fcp = Fluorcaphite, Kua-Ce = Kuannersuite-(Ce), Bri-Ce = Britholite-(Ce), Bri-Y = Britholite-(Y), Fbri-Nd = Fluorbritholite-(Nd), Clel = Chlorellestadite, Fel = Fluorellestadite, Mhd = Mattheddleite.

PM
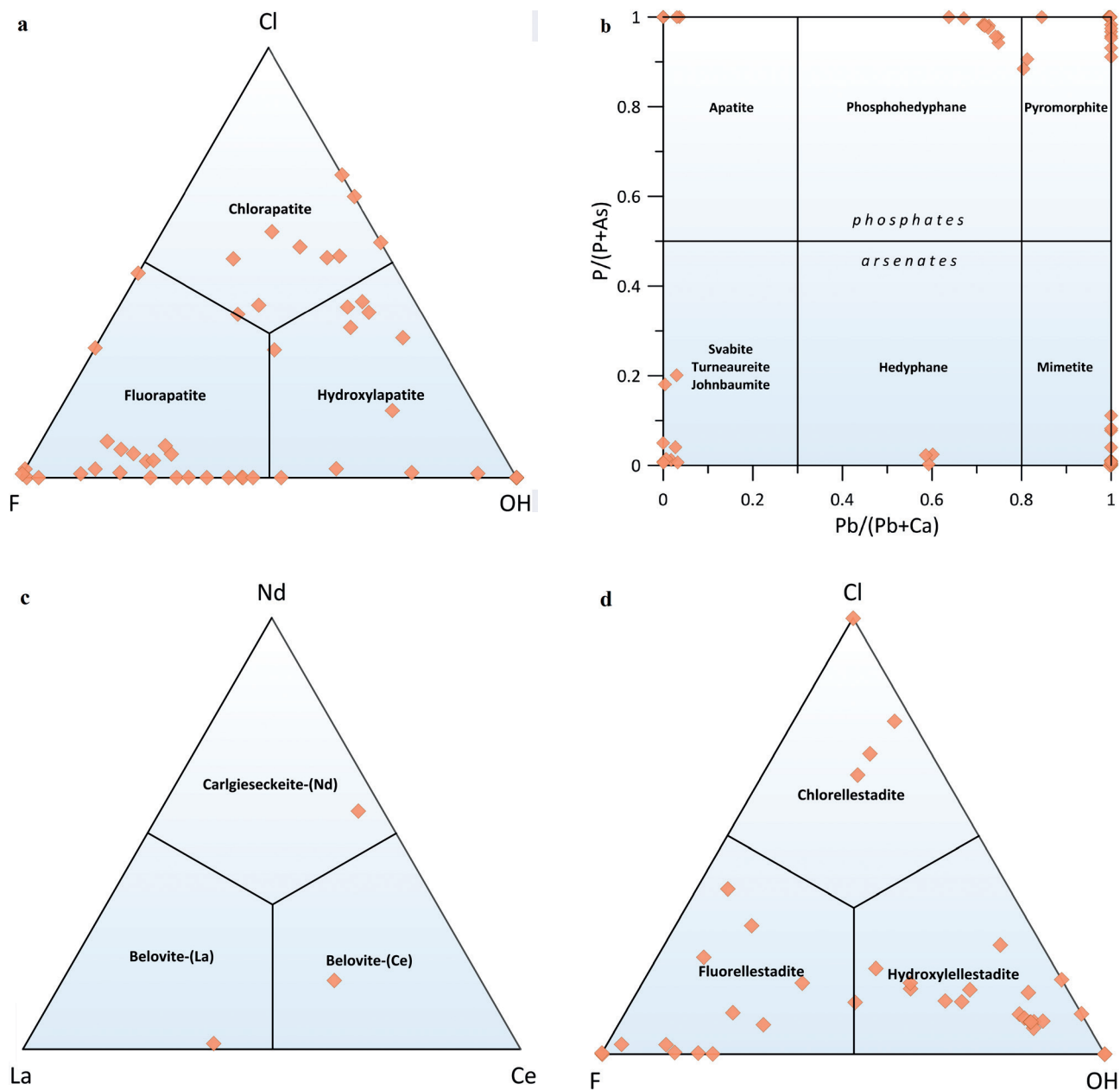
Figure 2. a) Classification of chlorapatite, fluorapatite and hydroxylapatite minerals in a ternary Cl–F–OH diagram (data from Broom-Fendley et al., 2016; Carrillo-Rosúa et al., 2021; Kruk et al., 2021; Piccoli and Candela 2002; Szuszkiewicz et al., 2018); b) Classification of some phosphate and arsenate apatite supergroup minerals in a binary Pb/(Pb+Ca) versus P/(P+As) diagram (from Vlasac et al., 2021; data from Sejorka et al., 2011; Dhaliwal, 2018; Henderson et al., 2009; Carrillo-Rosúa et al., 2021; Keim and Markl, 2017; Kruk et al., 2021; Biagioni et al., 2016); c) Classification of carlgieseckeite-(Nd), belovite-(La) and belovite-(Ce) minerals in a ternary Nd–La–Ce diagram (data from Rakovan and Hughes, 2000; Pekov et al., 2012; Anthony et al., 2001-2005); d) Classification of chlorellestadite, fluorellestadite and hydroxylellestadite minerals in a ternary Cl–F–OH diagram (data from Onac et al., 2006; Rouse and Dunn, 1982; Środek et al., 2018; Koděra et al., 2009; Kokh et al., 2015).

regions that affect the physical properties of silicate melts, control the eruptive styles and transporting metals such as Cu and Zn from silicic magmas to exsolved hydrothermal fluids in relation to ore deposits (McCubbin et al., 2015;

Chen et al., 2023). In an experimental study, Mathez and Webster (2005) investigated the partitioning behaviour of fluorine and chlorine in the apatite-mafic silicate melt-fluid system that conducted at 1066 to 1150 °C and 199
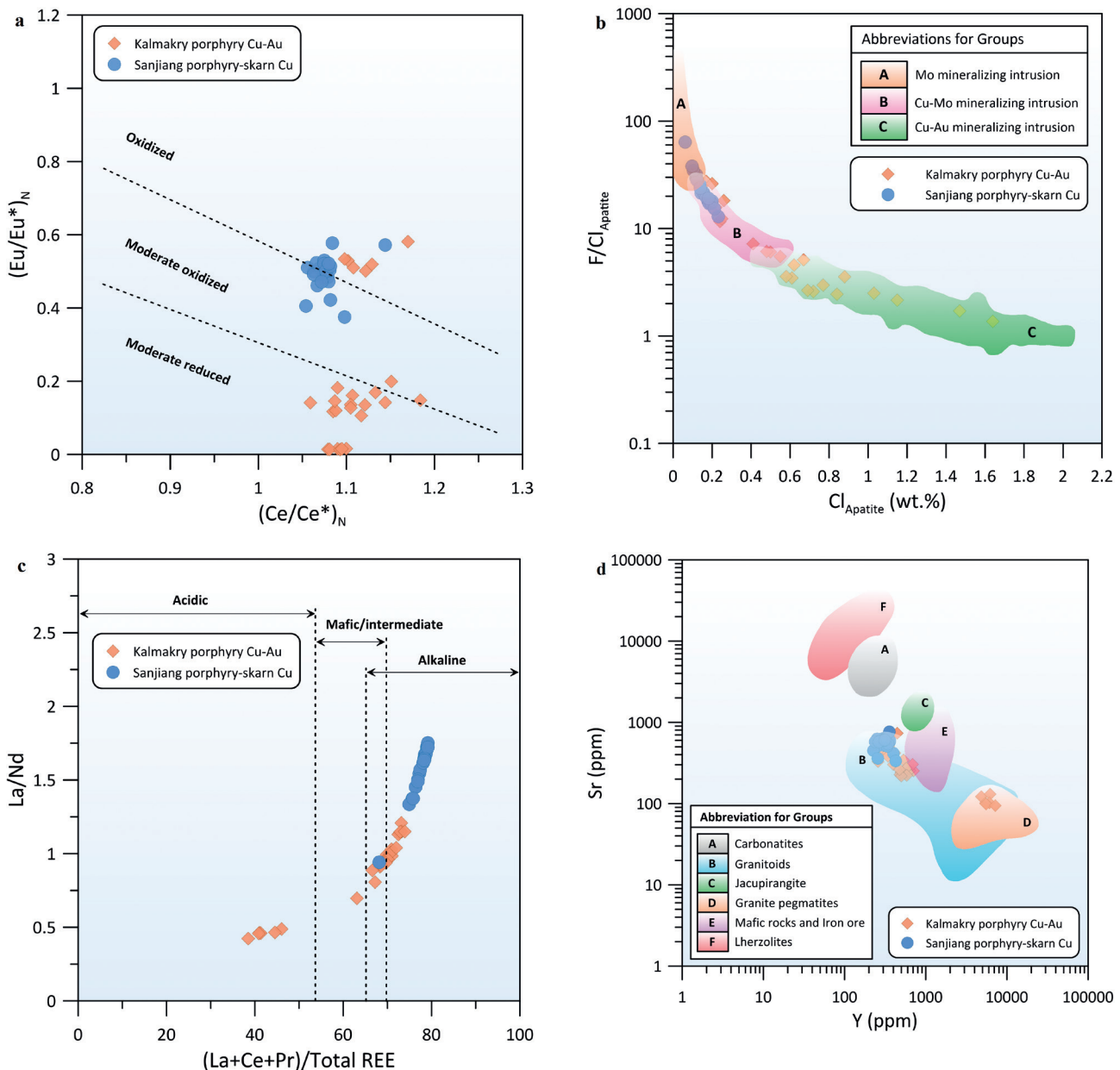
Figure 3. a) Distribution of apatite europium and cerium anomaly values in a binary $(Ce/Ce^*)_N$ versus $(Eu/Eu^*)_N$ diagram (from Cao et al., 2011; chondrite normalization values from Lodders, 2010); b) Plot of apatite compositions in a binary Cl versus F/Cl diagram (from Liu et al., 2023); c) Plot of apatite compositions in a binary (La+Ce+Pr)/Total REE versus La/Nd diagram (from Fleischer and Altschuler, 1986); d) Plot of apatite compositions in a binary Y versus Sr diagram (from Belousova et al., 2002).

to 205 MPa. The concentrations of Cl and F in apatite and coexisting melt at these conditions with $D_{Cl}^{Apatite/Melt} \approx 0.8$ and $D_F^{Apatite/Melt} \approx 3.4$ may be used to estimate the Cl and F concentrations of melt from Cl and F contents of apatite, respectively. Considering the partitioning of volatiles between apatite and silicate melts to be in a non-Nernstian behaviour, Li and Costa (2020) proposed a

thermodynamic model that allowing the non-ideal mixing in apatite solution with the interaction parameters (W_G) and Gibbs free energy properties based on the regressing experimental data taken from the literature. With the developed two equations, Li and Costa (2020) calculated the exchange coefficients (K_D) between apatite and silicate melts and established an online calculation procedure

PM
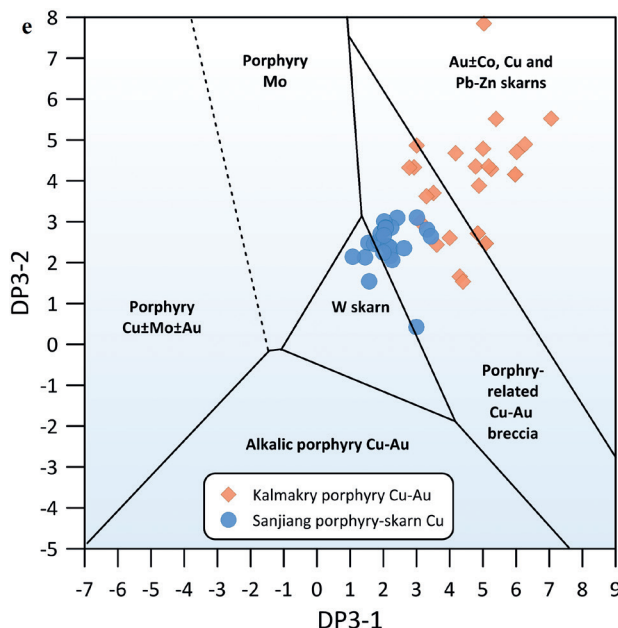
Figure 3. e) Plot of apatite compositions in a binary DP3-1 versus DP3-2 diagram (from Mao et al., 2002; discrimination boundaries from Rukhlov et al., 2016); f) Plot of apatite compositions in a binary LREE versus Sr/Y diagram (from O'Sullivan et al., 2020). All data used in Figure 3 are taken from Liu et al. (2023) and Liu et al. (2023).

for estimating the H_2O (wt%) in the melt (i.e., apatite hygrometer), with a relative uncertainty of 30-40%, that requires the knowledge of apatite chemistry as well as the Cl and F contents of melt. WinApclas lists the calculated Cl and F in melt contents (ppm) according to the models by Mathez and Webster (2005) and Li et al. (2021) for apatite compositions (see rows 40 to 43 in Table 6) in the *Calculation Screen* (i.e., in columns 156 to 159). The program also tabulates H_2O (wt%) amount in melt (see rows 44 to 46 in Table 6) on the basis of model proposed by Li and Costa (2020) in the *Calculation Screen* (i.e., in columns 160 to 162) for rhyolitic-dacitic, andesitic and basaltic magma type options selected from the pull-down menu of *Calculate H2O(melt)* in the *Data Entry Screen*.

Apatite, as S-bearing phosphate mineral, shows high resistance to alteration, weathering and diffusion processes. Apatite in volcanic rocks exhibits a wide range of SO_3 contents (<0.04 to 0.63 wt%). However, in hydrothermal ore deposits and hydrothermally altered rocks the crystal structure of apatite provides to contain up to 52.6 SO_3 (wt%) content (Peng et al., 1997). Although the S concentration in apatite is related to its crystallization with melt compositions, there is no formula to accurately calculate the S concentration of magma from the SO_3 content of apatite due to its formation is controlled by magma temperatures and oxidation state (Du et al., 2022). Nevertheless, if the chemical exchange between apatite and its host melt is ignored afterwards its formation, the relative S content of magma can be calculated using the semi-quantitative formulae proposed by Peng et al. (1997) and Parat et al. (2011). WinApclas lists the calculated S in melt contents (ppm) based on the models by Peng et al. (1997) and Parat et al. (2011) using apatite compositions (see rows 47 to 49 in Table 6) in the *Calculation Screen* (i.e., in columns 163 to 165).
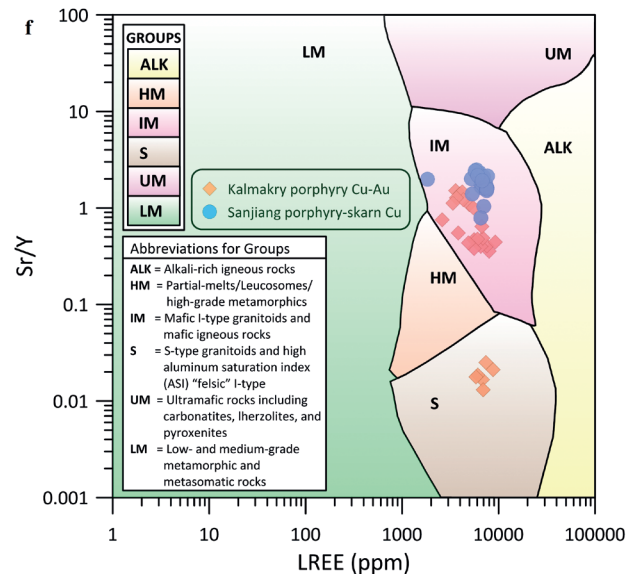
Magmatic water, pressure and magma reservoir depth estimations using apatite fluorine and chlorine contents for porphyry-related mineralization systems

Porphyry deposits, which are characterized by low-grade copper, gold, and/or molybdenum mineralization systems, are the major source of copper, gold, and molybdenum within and around a porphyritic intrusive complex in island arc and continental margin arc environments. Porphyry Cu deposits are generally associated with water-rich and oxidized magmas by reason of these characteristics contribute to the fruitful transfer of metals (e.g., Cu, Au) from magma composition into the aqueous phase (Jia et al., 2020; Zhang et al., 2022). Considering magmatic volatiles such as Cl and S play an important role in the formation of porphyry Cu-Mo-Au deposits that found in magmatic arcs above oceanic subduction zones (i.e., synsubduction setting) and in continent-collision or intracontinental settings

Table 6. Chemical compositions of selected hydroxylapatite analyses with their calculated parameters by WinApclas.

Row		S1	S2	S3	S4	S5	S6	S7	S8	S9	S10	S11	S12
1	SiO_2	0.310	0.160	0.240	0.100	0.100	0.080	0.090	0.070	0.090	0.110	0.450	0.280
2	La_2O_3	0.120	0.000	0.030	0.000	0.000	0.000	0.040	0.060	0.000	0.010	0.010	0.000
3	Ce_2O_3	0.100	0.020	0.040	0.070	0.040	0.030	0.110	0.070	0.090	0.080	0.070	0.120
4	P_2O_5	40.960	41.510	41.500	41.610	41.140	41.670	42.280	42.550	42.050	41.700	42.100	41.320
5	SO_3	0.000	0.000	0.010	0.030	0.020	0.010	0.020	0.030	0.000	0.000	0.000	0.000
6	MgO	0.190	0.210	0.240	0.190	0.230	0.260	0.230	0.250	0.220	0.190	0.230	0.220
7	FeO	0.570	0.580	0.540	0.620	0.550	0.580	0.660	0.530	0.620	0.550	0.640	0.570
8	MnO	0.080	0.110	0.140	0.120	0.150	0.120	0.140	0.100	0.170	0.140	0.130	0.140
9	CaO	53.210	53.080	53.550	53.620	54.370	54.550	53.570	53.670	54.070	53.990	53.520	53.230
10	Na_2O	0.010	0.040	0.090	0.050	0.050	0.030	0.020	0.030	0.060	0.040	0.030	0.020
11	F	0.970	0.950	0.950	1.010	1.350	1.170	0.960	1.050	1.180	1.310	0.990	0.940
12	Cl	1.670	1.690	1.700	1.670	1.340	1.320	1.430	1.440	1.430	1.450	1.580	1.670
13	$H_2O_{calculated}$	0.825	0.838	0.844	0.824	0.747	0.849	0.922	0.885	0.822	0.747	0.874	0.848
14	O=F	0.408	0.400	0.400	0.425	0.568	0.493	0.404	0.442	0.497	0.552	0.417	0.396
15	O=Cl	0.377	0.381	0.384	0.377	0.302	0.298	0.323	0.325	0.323	0.327	0.357	0.377
16	$\sum$ (wt%)	98.230	98.407	99.090	99.112	99.217	99.878	99.745	99.968	99.982	99.438	99.850	98.585
17	Si	0.027	0.014	0.021	0.009	0.009	0.007	0.008	0.006	0.008	0.009	0.039	0.024
18	La	0.004	0.000	0.001	0.000	0.000	0.000	0.001	0.002	0.000	0.000	0.000	0.000
19	Ce	0.003	0.001	0.001	0.002	0.001	0.001	0.003	0.002	0.003	0.003	0.002	0.004
20	P	3.041	3.068	3.051	3.057	3.022	3.041	3.083	3.088	3.059	3.048	3.062	3.053
21	S	0.000	0.000	0.001	0.002	0.001	0.001	0.001	0.002	0.000	0.000	0.000	0.000
22	Mg	0.025	0.027	0.031	0.025	0.030	0.033	0.030	0.032	0.028	0.024	0.029	0.029
23	Fe^{2+}	0.042	0.042	0.039	0.045	0.040	0.042	0.048	0.038	0.045	0.040	0.046	0.042
24	Mn	0.006	0.008	0.010	0.009	0.011	0.009	0.010	0.007	0.012	0.010	0.009	0.010
25	Ca	5.000	4.965	4.982	4.986	5.054	5.038	4.943	4.930	4.978	4.994	4.927	4.978
26	Na	0.002	0.007	0.015	0.008	0.008	0.005	0.003	0.005	0.010	0.007	0.005	0.003
27	$\sum$ (apfu)	8.150	8.131	8.153	8.143	8.176	8.177	8.130	8.112	8.143	8.136	8.120	8.143
28	X_F	0.269	0.262	0.261	0.277	0.370	0.319	0.261	0.285	0.321	0.358	0.269	0.259
29	X_{Cl}	0.248	0.250	0.250	0.246	0.197	0.193	0.209	0.209	0.208	0.212	0.230	0.247
30	X_{OH}	0.483	0.488	0.489	0.477	0.433	0.488	0.530	0.506	0.471	0.430	0.501	0.494
31	$\sum$ (apfu)	1.000	1.000	1.000	1.000	1.000	1.000	1.000	1.000	1.000	1.000	1.000	1.000
32	SiO_2 whole-rock (wt%)	69.34	69.34	69.54	69.54	67.57	67.57	67.60	67.60	67.46	67.46	69.46	69.46
33	P_2O_5 whole-rock (wt%)	0.14	0.14	0.14	0.14	0.19	0.19	0.19	0.19	0.19	0.19	0.14	0.14
34	T_{HW84} (°C)	935	934	936	936	950	949	948	947	947	948	933	936
35	T_{PC02} (°C)	933	933	935	935	948	948	949	949	947	947	934	934
36	$T_{Average}$ (°C)	934	933	935	935	949	949	948	948	947	947	934	935
37	Log fO_2	-11.11	-11.62	-12.14	-11.79	-12.31	-11.79	-12.14	-11.45	-12.65	-12.14	-11.97	-12.14

PM

Table 6. ... Continued

Row		S1	S2	S3	S4	S5	S6	S7	S8	S9	S10	S11	S12
38	FMQ	-11.96	-11.97	-11.94	-11.94	-11.71	-11.72	-11.73	-11.73	-11.75	-11.74	-11.96	-11.95
39	ΔFMQ	0.85	0.35	-0.20	0.15	-0.60	-0.08	-0.41	0.28	-0.90	-0.40	0.00	-0.19
40	$Cl_{(melt)\ MW05}$ (ppm)	1722	1741	1750	1722	1420	1401	1502	1511	1502	1521	1640	1722
41	$F_{(melt)\ MW05}$ (ppm)	241	234	234	254	369	307	238	267	310	355	247	231
42	$Cl_{(melt)\ LC20}$ (ppm)	1541	1537	1556	1544	1355	1190	1238	1283	1342	1484	1345	1512
43	$F_{(melt)\ LC20}$ (ppm)	224	215	216	236	419	308	224	256	314	394	218	212
44	$H_2O_{(melt)\ from\ Cl}$ (wt%)	1.51	1.52	1.52	1.50	1.35	1.38	1.45	1.43	1.40	1.38	1.47	1.51
45	$H_2O_{(melt)\ from\ F}$ (wt%)	1.40	1.39	1.39	1.42	1.67	1.55	1.42	1.46	1.53	1.62	1.42	1.39
46	$H_2O_{(melt)\ Average}$ (wt%)	1.45	1.45	1.45	1.46	1.51	1.46	1.43	1.44	1.47	1.50	1.45	1.45
47	$S_{(melt)\ P97}$ (ppm)	n.c.	n.c.	3	8	7	3	7	10	n.c.	n.c.	n.c.	n.c.
48	$S_{(melt)\ P11}$ (ppm)	n.c.	n.c.	20	23	22	20	22	23	n.c.	n.c.	n.c.	n.c.
49	$S_{(melt)\ Average}$ (ppm)	n.c.	n.c.	12	16	14	12	14	16	n.c.	n.c.	n.c.	n.c.

Samples (S1 to S12) from Du et al. (2022); The formulae were recalculated to 13 total anions; *apfu* = Atoms per formula unit; X_F, X_{Cl} and X_{OH} = Mole fractions of F, Cl and OH, respectively (rows 28to 30); Apatite Saturation Thermometers T_{HW14} by Harrison and Watson (1984), T_{PC02} by Piccoli and Candela (2002), $T_{Average}$ average of T_{HW14} and T_{PC02} (rows 34 to 36); Oxygen fugacity (*f*O$_2$) values (row 37) calculated from apatite composition using the model by Miles et al. (2014); Fayalite-Magnetite-Quartz (FMQ) values (row 38) using the model by Myers and Eugster (1983); Calculated ΔFMQ (row 39) by combining the model by Miles et al. (2014) and Myers and Eugster (1983); $Cl_{(melt)\ MW05}$ = Calculated Cl content (ppm) in the melt (row 40) using the model by Mathez and Webster (2005); $F_{(melt)\ MW05}$ = Calculated F content (ppm) in the melt (row 41) using the model by Mathez and Webster (2005); $Cl_{(melt)\ LC20}$ = Calculated Cl content (ppm) in the melt (row 42) using the model by Li and Costa (2020); $F_{(melt)\ LC20}$ = Calculated F content (ppm) in the melt (row 43) using the model by Li and Costa (2020); $H_2O_{(melt)\ from\ Cl}$ = Calculated H$_2$O content (wt.%) in the melt (row 44) from Cl using the model by Li and Costa (2020); $H_2O_{(melt)\ from\ F}$ = Calculated H$_2$O content (wt.%) in the melt (row 45) from F using the model by Li and Costa (2020); $H_2O_{(melt)\ Average}$ = Average H$_2$O content (wt%) in the melt (row 46) from Cl and F using the model by Li and Costa (2020); $S_{(melt)\ P97}$ = Calculated S content (ppm) in the melt (row 47) using the model by Peng et al. (1997); $S_{(melt)\ P11}$ = Calculated S content (ppm) in the melt (row 48) using the model by Parat et al. (2011); $S_{(melt)\ Average}$ = Average S content (ppm) in the melt (row 49) using the models by Peng et al. (1997) and Parat et al. (2011); n.c. = not calculated (i.e., Because of the absent SO$_3$ (wt%) values in the apatite analyses).

(i.e., postsubduction setting), Huang et al. (2023) compiled existing chemical data of magmatic apatite and amphibole phenocrysts from 25 porphyry Cu deposits worldwide (i.e., over 1000 published compositions) and used these data to calculate magmatic physical-chemical conditions (e.g., water contents and magma reservoir depths). According to Huang et al. (2023), the porphyry Cu deposits associated with deeper magma reservoirs show systematically higher magmatic H$_2$O and apatite Cl contents when compared to the lower apatite F contents and F/Cl ratios in shallower deposits. They also showed that the apatite volatile composition and

magma reservoir depth exhibit significant differences between synsubduction and postsubduction porphyry Cu systems that can be explained to express contrasting tectonic regimes during their formations. In conclusion, considering positive correlation between the apatite Cl contents with magmatic water contents and reservoir depth as well as negative correlations between the apatite F contents and F/Cl ratios with both magmatic water contents and magma reservoir depth relations, which are observed by Huang et al. (2023), WinApclas estimates and lists the magmatic water contents (wt%), crystallization pressure (kbar) and depth (km) values for

apatite compositions from porphyr Cu and related ore deposits in the *Calculation Screen* (i.e., in columns 167 to 178). These estimated values by program should only be used for apatite compositions obtained from porphyry-related mineralised systems (see rows 28 to 39 in Table 7) with cautious due to low to moderate empirical correlations between the apatite F and Cl contents and the estimated H_2O_{melt} (wt%), pressure (*P*, kbar) and depth (km) parameters that are based on the semi-quantitative regression relationships proposed by Huang et al. (2023).

Apatite chemistry in provenance and mineral exploration studies

As an important indicator mineral, apatite's large compositional variability is used in specific provenance and mineral exploration studies due to its: ubiquitous behaviour in crystalline rocks, variable trace and REE contents that at least partly controlled by the host rock chemistry and in various dating techniques based on the decay of the radioisotopes U and Th (O'Sullivan et al., 2020). For example, in order to understand the origin of apatite in different types of granitic rocks, contents of Na, Ca, Sr, Cr, and Ni, REE patterns as well as element ratios (e.g., La/Y, Sm/Nd, Fe^{3+}/Fe^{2+}) are used for discrimination purposes (Tan et al., 2023). Fleischer and Altschuler (1986) used apatite compositions associated with acidic, mafic/intermediate and alkaline rocks in La/Nd versus (La+Ce+Pr)/ΣREE plot to show realistic interpretation of source area lithology (Figure 3c). In this context, Dill (1994) was the first to apply apatite REE and actinide chemistry of southern Germany as a detrital provenance tool that further to use this knowledge in identifying the Permo-Triassic clastic successions. Belousova et al. (2002) investigated the potential usefulness of apatite compositions as an indicator mineral in mineral exploration with different binary discriminant plots (e.g., Y-SR, Mn-Sr, Eu/Eu*-Y, ΣREE-(Ce/Yb)$_{cn}$) based on over 700 laser-ablation microprobe ICPMS apatite grain analyses from a range of rock types (i.e., granitoids, granite pegmatite, dolerite, lherzolite, carbonatite, larvikite and jacpirangite) to identify fields of apatite compositions (Figure 3d). Using single detrial grains laser-ablation inductively coupled plasma-mass spectrometry apatite compositions from Pliocene sandstones in the South Caspian Basin (Azerbaijan) and Devonian-Carboniferous sandstones from Clair oil field (UK), Morton and Yaxley (2007) demonstrated that apatite geochemistry can be used potentially in provenance analysis. Teiber et al. (2015) used electron-microprobe (EPMA) and total reflection X-ray fluorescence (TXRF) analyses on 17 apatite samples from magmatic to hydrothermal origin (e.g., carbonatites, ijolites, silico-carbonatic pegmatites and Kiruna-type deposit) and compared visually their major oxide and halogen (wt%) as well as trace and REE (ppm) contents in binary and ternary diagrams with a compilation of literature data for apatite compositions from carbonatites, gabbros, diorites, biotite (± amphibole) -bearing granitoids, muscovite-bearing granites, felsic pegmatites and the widely known Durango apatite. Similarly, Mao et al. (2016) analysed a total of 922 apatite compositions for 902 grains from the major types of commonly magmatic-hydrothermal mineral deposits (i.e., 30 localities), carbonatites (i.e., 29 intrusive complexes) and unmineralized rocks (i.e., 11 localities) using electron-microprobe and laser ablation-inductively coupled plasma mass spectrometry and applied a Discriminant Projection Analysis (DPA) technique to the results of trace element contents including Mg, V, Mn, Sr, Y, La, Ce, Eu, Dy, Yb, Pb, Th and U for discriminating barren rocks and various ore deposit types in different discriminant functions (see Figure 3e). Rukhlov et al. (2016), in a first test of the apatite classification by Mao et al. (2016), used EMPA and LA-ICP-MS examination of 147 apatite grains taken from 14 till samples at the Highland Valley, Gibraltar, Mount Polley, and Woodjam porphyry deposits, and from two mineralized bedrock samples at the Woodjam Southeast Zone, observed systematic trace-element patterns characteristic in terms of the degree of fractionation and the relative redox state of magmatic-hydrothermal ore systems and showed that apatite trace-element chemistry can be used as an effective mineral exploration tool. Considering the correlation between texture, luminescence as well as chemical composition relationships with the type and intensity of porphyry alteration systems, Bouzari et al. (2016) used cathodoluminescence combined with trace element contents of apatite compositions from porphyry copper deposits to discriminate trace element variations from alteration events to utilize this situation as an indicator for porphyry mineralization in a range of exploration materials for soils, regoliths and heavy mineral concentrates from glacial and fluvial environments. O'Sullivan et al. (2020) investigated a comprehensive description of the trace element behaviour of apatite in various bedrock compositions (e.g., igneous, metamorphic and authigenic apatite), presented a synthesis of bedrock apatite trace-element compositional data from previous work and applied compositional statistics such as Principal Component Analysis (PCA) and a machine learning method of Support Vector Machine (SVM) to the related dataset to generate Sr/Y vs ΣLREE biplot which is found to be a simple tool for discrimination of the broad provenance of detrital apatite in six common lithologies (i.e., low- and medium-grade metamorphic apatite, high-grade metamorphic apatite, felsic granitoids, mafic granitoids and mafic igneous apatite, alkali-rich igneous apatite and ultramafic-carbonatitic apatite) with various degrees of overlap (Figure 3f).

Table 7. Chemical compositions of selected fluorapatite analyses from porphyry-related mineralization systems with their calculated parameters by WinApclas.

Row		S1ss	S2ss	S3ss	S4ss	S5ss	S6ss	S7ps	S8ps	S9ps	S10ps	S11ps	S12ps
1	SiO_2	0.150	0.010	0.000	0.350	0.170	1.150	0.250	0.480	0.550	0.150	0.170	0.370
2	P_2O_5	42.940	41.730	40.990	41.710	42.120	40.220	41.780	41.190	40.730	42.070	42.490	40.660
3	SO_3	0.140	0.020	0.200	0.310	0.250	0.410	0.180	0.450	0.440	0.130	0.200	0.200
4	MgO	0.010	0.000	0.000	0.000	0.000	0.000	0.000	0.010	0.000	0.000	0.010	0.020
5	FeO	0.030	0.080	0.000	0.180	0.140	0.100	0.040	0.030	0.000	0.000	0.000	0.090
6	MnO	0.030	0.390	0.000	0.310	0.000	0.120	0.170	0.040	0.070	0.200	0.010	0.010
7	CaO	54.130	55.390	54.040	54.270	55.900	54.270	54.410	54.480	53.520	54.360	54.340	54.850
8	Na_2O	0.030	0.040	0.120	0.100	0.080	0.000	0.060	0.080	0.120	0.000	0.080	0.300
9	F	3.060	2.230	2.040	1.610	2.500	2.360	2.690	2.970	2.970	3.220	3.120	3.290
10	Cl	0.350	1.000	1.310	1.930	0.580	1.270	0.440	0.360	0.250	0.300	0.170	0.050
11	$H_2O_{calculated}$	0.245	0.448	0.425	0.505	0.452	0.305	0.371	0.261	0.266	0.167	0.256	0.176
12	O=F	1.288	0.939	0.859	0.678	1.053	0.994	1.133	1.251	1.251	1.356	1.314	1.385
13	O=Cl	0.079	0.226	0.296	0.435	0.131	0.287	0.099	0.081	0.056	0.068	0.038	0.011
14	$\sum$ (wt%)	99.748	100.173	97.970	100.162	101.008	98.924	99.159	99.019	97.609	99.173	99.494	98.620
15	Si	0.013	0.001	0.000	0.030	0.014	0.099	0.021	0.041	0.047	0.013	0.014	0.032
16	P	3.054	3.011	3.016	3.010	2.995	2.922	3.015	2.969	2.974	3.017	3.031	2.951
17	S	0.009	0.001	0.013	0.020	0.016	0.026	0.012	0.029	0.028	0.008	0.013	0.013
18	Mg	0.001	0.000	0.000	0.000	0.000	0.000	0.000	0.001	0.000	0.000	0.001	0.003
19	Fe^{2+}	0.002	0.006	0.000	0.013	0.010	0.007	0.003	0.002	0.000	0.000	0.000	0.006
20	Mn	0.002	0.028	0.000	0.022	0.000	0.009	0.012	0.003	0.005	0.014	0.001	0.001
21	Ca	4.873	5.058	5.033	4.956	5.030	4.990	4.970	4.970	4.946	4.934	4.907	5.037
22	Na	0.005	0.007	0.020	0.017	0.013	0.000	0.010	0.013	0.020	0.000	0.013	0.050
23	$\sum$ (apfu)	7.959	8.111	8.083	8.068	8.089	8.053	8.043	8.029	8.021	7.990	7.988	8.092
24	X_F	0.813	0.601	0.561	0.434	0.664	0.641	0.725	0.800	0.810	0.863	0.832	0.892
25	X_{Cl}	0.050	0.144	0.193	0.279	0.083	0.185	0.064	0.052	0.037	0.043	0.024	0.007
26	X_{OH}	0.137	0.255	0.246	0.287	0.253	0.175	0.211	0.148	0.153	0.094	0.144	0.101
27	$\sum$ (apfu)	1.000	1.000	1.000	1.000	1.000	1.000	1.000	1.000	1.000	1.000	1.000	1.000
28	H_2O_{melt} from Cl_{Ap} (wt%)	3.99	4.60	4.88	5.46	4.21	4.85	4.08	4.00	3.90	3.95	3.83	3.72
29	H_2O_{melt} from F_{Ap} (wt%)	3.85	4.90	5.14	5.68	4.56	4.73	4.32	3.96	3.96	3.65	3.77	3.56
30	H_2O_{melt} from $(F/Cl)_{Ap}$ (wt%)	4.38	4.99	5.15	5.43	4.69	5.07	4.54	4.40	4.24	4.28	4.04	3.47
31	Average H_2O_{melt} (wt%)	4.07	4.83	5.06	5.52	4.49	4.88	4.31	4.12	4.03	3.96	3.88	3.58
32	P from Cl_{Ap} (kbar)	2.13	2.51	2.69	3.05	2.27	2.67	2.19	2.14	2.07	2.10	2.03	1.96
33	P from F_{Ap} (kbar)	1.88	2.64	2.82	3.21	2.39	2.52	2.22	1.96	1.96	1.73	1.82	1.66
34	P from $(F/Cl)_{Ap}$ (kbar)	2.28	2.70	2.81	3.00	2.50	2.76	2.39	2.30	2.18	2.22	2.05	1.65
35	Average P (kbar)	2.10	2.62	2.77	3.09	2.39	2.65	2.26	2.13	2.07	2.02	1.97	1.76
36	Depth from Cl_{Ap} (km)	7.76	9.33	10.08	11.58	8.32	9.98	7.98	7.78	7.52	7.64	7.32	7.03
37	Depth from F_{Ap} (km)	7.35	10.16	10.80	12.26	9.24	9.72	8.60	7.65	7.65	6.80	7.14	6.57
38	Depth from $(F/Cl)_{Ap}$ (km)	8.55	10.15	10.57	11.30	9.38	10.36	8.97	8.62	8.19	8.31	7.68	6.18
39	Average depth (km)	7.88	9.88	10.48	11.71	8.98	10.02	8.52	8.02	7.79	7.58	7.38	6.59

Samples (S1ss to S12ps) from Huang et al. (2023); ss = Subduction setting, ps = Postsubduction setting; S1ss = Baogutu porphyry Cu, S2ss = Xiongcun porphyry Cu-Au, S3ss = Santa Rita porphyry Cu, S4ss = Duolong porphyry-epithermal Cu-Au, S5ss = Coroccohuayco porphyry-skarn Fe-Cu-Au, S6ss = Red Chris porphyry Au, S7ps = Niutoushan porphyry-skarn Cu, S8ps = Fuzishan porphyry-skarn Cu-Au, S9ps = Ouyangshan porphyry-skarn Cu, S10ps = Qulong porphyry Cu-Mo, S11ps = Pulang porphyry Cu-Au, S12ps = Tongchang porphyry Cu-Mo; The formulae were recalculated to 13 total anions; apfu = Atoms per formula unit; X_F, X_{Cl} and X_{OH} = Mole fractions of F, Cl and OH, respectively (rows 24 to 27); Estimations of H_2O (rows 28 to 30) in melt (H_2O_{melt}) from Cl and F contents of apatite (Cl_{Ap} and F_{Ap}) and $(F/Cl)_{Ap}$ ratio are based on the empirical correlation relationships by Huang et al. (2023); Estimations of pressure (P, kbar) values (rows 32 to 34) from Cl and F contents of apatite (Cl_{Ap} and F_{Ap}) and $(F/Cl)_{Ap}$ ratio are based on the empirical correlation relationships by Huang et al. (2023); Estimations of depth (km) values (rows 36 to 38) from Cl and F contents of apatite (Cl_{Ap} and F_{Ap}) and $(F/Cl)_{Ap}$ ratio are based on the empirical correlation relationships by Huang et al. (2023).

Considering the complex chemistry of apatite and the natural difficulty of binary or ternary discrimination diagrams in distinguishing the genetic types of apatite, Zhou et al. (2023) collected worldwide previously published 1551 mineralized apatite LA-ICP-MS analyses from an open-access apatite trace element dataset (i.e., La, Ce, Pr, Nd, Sm, Eu, Gd, Dy, Yb, Lu, Sr, Y, Th and U) belonging to five common ore deposit types such as porphyry, skarn, orogenic Au, iron-oxide copper gold (IOCG) and iron-oxide apatite (IOA or Kiruna type) deposit and provided a novel machine learning visualization method that combines Supervised Decision Boundary Maps (SDBM) and Attribute-based visual explanation of Multidimensional Projections (A-MPs) to investigate the genesis classification of apatite with a high accuracy and strong interpretability purposes. Tan et al. (2023) collected a total of 4298 apatite data from different types of deposits and rocks, divided them into a several categories (e.g., magmatic, hydrothermal, barren, mineralized, deposit and rock types), applied the method of Partial least squares-discriminant analysis to classify apatite compositions in different origins and proposed a flowchart for discriminating apatite with unknown origins both in mineral explorations and factors controlling magmatic and hydrothermal processes. On the other hand, using a supervised machine learning-based methodology (i.e., eXtreme Gradient Boosting-XGBoost), Qui et al. (in press) evaluated 8629 apatite trace element compositional data associated with five ore deposit types including porphyry, skarn, orogenic Au, iron oxide copper gold and iron oxide-apatite to identify discriminating parameters both for unmineralized magmatic and metamorphic as well as mineralized systems. Based on the selected elements (i.e., Th, U, Sr, Eu, Dy, Y, Nd and La), they proposed that the XGBoost algorithm accurately and efficiently classifies apatite with ore deposit type (overall accuracy >94%) and yields the optimal elements (Th, U, Eu and Nd) to discriminate apatite from different ore deposit types.

SUMMARY AND AVAILABILITY OF THE PROGRAM

The atomic arrangement of apatite as well as its variable chemical composition and widespread distribution as the most abundant phosphate mineral on Earth together with its stable behaviour in a wide variety of conditions from the Earth's surface to the lithospheric mantle have resulted in many fields of applications such as agronomy, mineralogy, petrology, economic geology, biology, medicine, dentistry, geochronology, environmental remediation and materials science (Hughes and Rakovan, 2015). WinApclas is a user-friendly program which is specially developed for personal computers running on the Windows operating system to estimate and classify the apatite supergroup mineral compositions obtained from both electron-microprobe and wet chemical analyses. The program calculates multiple analyses, up to 200, for each program execution. WinApclas evaluates the apatite supergroup mineral analyses into five groups such as pyroclore apatite, hedyphane, belovite, britholite and ellestadite based on the current IMA-approved nomenclature scheme and then classifies the total 47 species according to the dominant ions at the M, T and X sites in the shortly $M_5(TO_4)_3X$ formula. The program generates two main windows. The first window (i.e., Start-up/Data Entry Screen), with several pull-down menus and equivalent shortcuts, enables to edit apatite supergroup analyses (wt%) in 54 columns. By clicking the Calculate icon (i.e., $\sum$) in the Data Entry Screen, all input and estimated parameters by WinApclas are displayed in the second window (i.e., Calculation Screen). The program reports the output in a tabulated form with a numbered column number from 1 to 178 in the Calculation Screen window as well as in an Output Excel file. These columns cover apatite and whole-rock or melt input compositions and program's output parameter such as the calculated H_2O (wt%) contents based on the stoichiometric constraints, recalculated cation and anion values together with the mole fractions of F, Cl and OH (i.e., X_F, X_{Cl} and X_{OH}) values, total M and T site contents with their total charges, cerium and europium anomalies [i.e., $(Ce/Ce^*)_N$, $(Eu/Eu^*)_N$], dominant M, T and X site components, group and species names, apatite saturation temperature (^oC) values, oxygen fugacity (fO_2), fayalite-magnetite-quartz buffer (FMQ) and relative oxygen fugacity (ΔFMQ) values as well as the calculated Cl, F, S (ppm) and H_2O (wt%) contents in the melt. The results in the Calculation Screen can be exported to a Microsoft® Excel file (i.e., Output.xlsx), by clicking the Send Results to Excel File (Output.xlsx) icon or selecting the Send Results to Excel File (Output.xlsx) option from the pull-down menu of Excel and then this file is opened by Excel by clicking the Open and Edit Excel File (Output.xlsx) icon or selecting the Open Excel File (Output.xlsx) option from the pull-down menu of Excel. WinPclclas is a compiled program that consists of a self-extracting setup file containing all the necessary support files (i.e., dll and ocx) for the 32-bit system. By clicking the setup file, the program and its associated files (i.e., support files, help file, data files with the extension of aps, xls, xlsx and plot files with the extension of ".grf" are installed into the personal computer (i.e., the directory of C:\Program Files\WinApclas or C:\Program Files (x86)\WinApclas) with the Windows XP and later operating systems. An installation of the program into a personal computer with the 64-bit operating system may require the msflexgrd adjustment. The self-extracting setup file is approximately 17 Mb and can be obtained from the journal's server as a Supplementary Material.

PM

REFERENCES

Andersson S.S., Wagner T., Jonsson E., Fusswinkel T., Whitehouse M.J., 2019. Apatite as a tracer of the source, chemistry and evolution of ore-forming fluids: The case of the Olserum-Djupedal REE-phosphate mineralisation, SE Sweden. Geochimica et Cosmochimica Acta 255, 163-187.

Anthony J.W., Bideaux R.A., Bladh K.W., Nichols M.C., 2001-2005. Handbook of Mineralogy, Mineralogical Society of America, Chantilly, VA 20151-1110, USA. http://www.handbookofmineralogy.org/.

Bačík P., Fridrichová J., Štubňa J., Bancík T., Illášová, Ĺ., Pálková H., Škoda R., Mikuš T., Milovská S., Vaculovič T., Sečkár P., 2020. The REE-induced absorption and luminescence in yellow gem-quality durango-type hydroxylapatite from Muránska Dlhá Lúka, Slovakia. Minerals 10, 1001.

Belousova E.A., Griffin W.L., O'Reilly S.Y., Fisher N.I., 2002. Apatite as an indicator mineral for mineral exploration: trace-element compositions and their relationship to host rock type. Journal of Geochemical Exploration 76, 45-69.

Biagioni C., Bosi F., Hålenius U., Pasero M., 2016. The crystal structure of svabite, Ca5(AsO4)3F, an arsenate member of the apatite supergroup. American Mineralogist 101, 1750-1755.

Bouzari F., Hart C.J.R., Bissig T., Barker S., 2016. Hydrothermal alteration revealed by apatite luminescence and chemistry: A potential indicator mineral for exploring covered porphyry copper deposits. Economic Geology 111, 1397-1410.

Broom-Fendley S., Styles, M.T., Appleton, J.D., Gunn, G., Wall, F., 2016. Evidence for dissolution-reprecipitation of apatite and preferential LREE mobility in carbonatite-derived late-stage hydrothermal processes. American Mineralogist 101, 596-611.

Carrillo-Rosúa J., Esteban-Arispe I., Morales-Ruano S., 2021. Anion composition of apatite in the Au-Cu epithermal deposit of Palai-Islica (Almería, SE Spain) as an indicator of hydrothermal alteration. Minerals 11, 1358.

Cavarretta G., Mottana A., Tecce F., 1981. Cesanite, Ca2Na3[(OH)(SO4)3], a sulphate isotypic to apatite, from the Cesano geothermal field (Latium, Italy). Mineralogical Magazine 44, 269-273.

Chakhmouradian A.R., Hughes J.M., Rakovan J., 2005. Fluorcaphite, a second occurrence and detailed structural analysis: Simultaneous accommodation of Ca, Sr, Na, and LREE in the apatite atomic arrangement. Canadian Mineralogist 43, 735-746.

Chen X., Leng C.B., Zou S., Li K., Zhang L., 2021. Geochemical compositions of apatites from the Xuejiping and Disuga porphyries in Zhongdian arc: Implications for porphyry Cu mineralization. Ore Geology Reviews 130, 103954.

Chen Z., Tamehe L.S., Qi H., Zhang Y., Zeng Z., Cai M., 2023. Using apatite to track volatile evolution in the shallow magma chamber below the Yonaguni Knoll IV hydrothermal field in the southwestern Okinawa Trough. Journal of Marine Science and Engineering 11, 583.

Chew D.M. and Spikings R.A., 2021. Apatite U-Pb thermochronology: A review. Minerals 11, 1095.

Dhaliwal I., 2018. Structure and chemistry of pyromorphite, Pb5(PO4)3Cl, mimetite, Pb5(AsO4)3Cl, vanadinite, Pb5(VO4)3Cl, and erythrite, Co3(AsO4)28H2O. (Unpublished Master's Thesis). University of Calgary, Calgary, 106 pp. doi: 10.11575/PRISM/13064.

Du X., Zeng Z., Chen Z., 2022. Volatile characteristics of apatite in dacite from the Eastern Manus Basin and their geological implications. Journal of Marine Science and Engineering 10, 698.

Dunn P.J., Peacor D.R., Newberry N., 1980. Johnbaumite, a new member of the apatite group from Franklin, New Jersey. American Mineralogist 65, 1143-1145.

Fleischer M. and Altschuler Z.S., 1986. The lanthanides and yttrium in minerals of the apatite group-An analysis of the available data. Neues Jahrbuch für Mineralogie Abhandlungen 10, 467-480.

Frost R.B., 1991. Introduction to oxygen fugacity and its petrological importance. In: Oxide Minerals: Petrologic and Magnetic Significance. (Ed.): D.H. Lindsley. Reviews in Mineralogy and Geochemistry 25, 1-8.

Harrison T.M. and Watson E.B., 1984. The behavior of apatite during crustal anatexis: Equilibrium and kinetic considerations. Geochimica et Cosmochimica Acta 48, 1467-1477.

Henderson C.M.B., Bell A.M.T., Charnock J.M., Knight K.S., Wendlandt R.F., Plant D.A., Harrison W.J., 2009. Synchrotron X-ray absorption spectroscopy and X-ray powder diffraction studies of the structure of johnbaumite [Ca10(AsO4)6(OH,F)2] and synthetic Pb-, Sr- and Ba-arsenate apatites and some comments on the crystal chemistry of the apatite structure type in general. Mineralogical Magazine 73, 433-455.

Holtstam D., Casey P., Bindi L., Förster H.J., Karlsson A., Appelt O., in press. Fluorbritholite-(Nd), Ca2Nd3(SiO4)3F, a new and a key mineral for neodymium sequestration in REE skarns. Mineralogical Magazine.

Huang M.L., Zhu J.J., Chiaradia M., Hu R.Z., Xu L.L., Bi X.W., 2023. Apatite volatile contents of porphyry Cu deposits controlled by depth-related fluid exsolution processes. Economic Geology 118, 1201-1217.

Hughes J.M. and Rakovan J.F., 2015. Structurally robust, chemically diverse: Apatite and apatite supergroup minerals. Elements 11, 165-170.

Jia F., Zhang C., Liua H., Meng X., Kong Z., 2020. In situ major and trace element compositions of apatite from the Yangla skarn Cu deposit, southwest China: Implications for petrogenesis and mineralization. Ore Geology Review 127, 103360.

Kampf A.R., Steele I.M., Jenkins R.A., 2006. Phosphohedyphane, $Ca_2Pb_3(PO_4)_3Cl$, the phosphate analog of hedyphane: Description and crystal structure. American Mineralogist 91, 1909-1917.

Kasatkin A.V., Pekov I.V., Škoda R., Chukanov N.V., Nestola F., Agakhanov A.A., Kuznetsov A.M., Koshlyakova N.N., Plášil J., Britvin S.N., 2023. Fluorpyromorphite, $Pb_5(PO_4)_3F$, a new apatite-group mineral from Sukhovyaz Mountain, Southern Urals, and Tolbachik volcano, Kamchatka. Journal of Geosciences 68, 81-93.

Keim M.F. and Markl G., 2017. Formation of galena pseudomorphs after pyromorphite. Neues Jahrbuch für Mineralogie Abhandlungen 194, 209-226.

Ketcham R.A., 2015. Calculation of stoichiometry from EMP data for apatite and other phases with mixing on monovalent anion sites. American Mineralogist 100, 1620-1623.

Koděra P., Uher P., Ozdín D., Kollárová V., Lexa J., 2009. Monticellite, clintonite and hydroxylellestadite to fluorellestadite: Rare skarn minerals of the Vysoká-Zlatno Cu-Au porphyry-skarn deposit (Štiavnica stratovolcano, Slovakia). Mineralia Slovaca 41, 169-178.

Kokh S.N., Sokol E.V., Sharygin V.V., 2015. Ellestadite-group minerals in combustion metamorphic rocks. Coal and Peat Fires: A Global Perspective. (Eds.): G.B. Stracher, A. Prakash and E.V. Sokol, 544-562.

Kress V.C. and Carmichael I.S.E., 1991. The compressibility of silicate liquids containing Fe_2O_3 and the effect of composition, temperature, oxygen fugacity and pressure. Contributions to Mineralogy and Petrology 108, 82-92.

Kruk M.N., Doroshkevich A.G., Prokopyev I.R., Izbrodin I.A., 2021. Mineralogy of phoscorites of the Arbarastakh Complex (Republic of Sakha, Yakutia, Russia). Minerals 11, 556.

Krzątała A., Skrzyńska K., Cametti G., Galuskina I., Vapnik Y., Galuskin E., in press. Fluoralforsite, $Ba_5(PO_4)_3F$ - a new apatite group mineral from the Hatrurim Basin, Negev Desert, Israel. Mineralogical Magazine.

Liu Q., Pan L.C., Wang X.S., Yan J., Xing L.Z., 2023. Apatite geochemistry as a proxy for porphyry-skarn Cu genesis: a case study from the Sanjiang region of SW China. Frontiers in Earth Science 11, 1185964.

Liu Y., Zhao X., Xue C., Nurtaev B., Chen J., 2023. Contrasting apatite geochemistry between ore-bearing and ore-barren intrusions of the giant Kalmakyr gold-rich porphyry Cu deposit, Tien Shan, Uzbekistan. Frontiers in Earth Science 11, 1162994.

Li W. and Costa F., 2020. A thermodynamic model for F-Cl-OH partitioning between silicate melts and apatite including non-ideal mixing with application to constraining melt volatile budgets. Geochimica et Cosmochimica Acta 269, 203-222.

Li W., Costa F., Nagashima K., 2021. Apatite crystals Reveal melt volatile budgets and magma storage depths at Merapi Volcano, Indonesia. Journal of Petrology 62, egaa100.

Lodders K., 2010. Solar system abundances of the elements. In: Principles and Perspectives in Cosmochemistry. (Eds.): A. Goswami and B.E. Reddy, Kodai School on Synthesis of Elements in Stars, Kodaikanal Observatory, India, April 29-May 13, 2008, Berlin, Heidelberg, Springer Verlag, Lecture Notes, 379-417.

London D., Wolf M.B., Morgan G.B.V.I., Garrido M.G., 1999. Experimental silicate-phosphate equilibria in peraluminous granitic magmas, with a case study of Albuquerque Batholith at Tres Arroyos, Badajoz, Spain. Journal of Petrology 40, 215-240.

Mao M., Rukhlov A.S., Rowins S.M., Spence J., Coogan L.A., 2016. Apatite trace element compositions: A robust new tool for mineral exploration. Economic Geology 111, 1187-1222.

Marks M.A.W., Scharrer M., Ladenburger S., Markl G., 2016. Comment on ''Apatite: A new redox proxy for silicic magmas?''. Geochimica et Cosmochimica Acta 183, 267-270.

Mathez E.A. and Webster J.D., 2005. Partitioning behavior of chlorine and fluorine in the system apatite-silicate melt-fluid. Geochimica et Cosmochimica Acta 69, 1275-1286.

McCubbin F.M., Vander Kaaden K.E., Tartèse R., Boyce J.W., Mikhail S., Whitson E.S., Bell A.S., Anand M., Franchi I.A., Wang J., Hauri E.H., 2015. Experimental investigation of F, Cl, and OH partitioning between apatite and Fe-rich basaltic melt at 1.0-1.2 GPa and 950-1000 °C. American Mineralogist 100, 1790-1802.

Miles A.J., Graham C.M., Hawkesworth C.J., Gillespie M.R., Hinton R.W., Bromiley G.D., 2014. Apatite: A new redox proxy for silicic magmas? Geochimica et Cosmochimica Acta 132, 101-119.

Miles A.J., Graham C.M., Hawkesworth C.J., Gillespie M.R., Hinton R.W., Bromiley G.D., 2016. Reply to comment by Marks et al. (2016) on ''Apatite: A new redox proxy for silicic magmas?''. Geochimica et Cosmochimica Acta 183, 271-273.

Morton A. and Yaxley G., 2007. Detrital apatite geochemistry and its application in provenance studies. In: Sedimentary Provenance and Petrogenesis. (Eds.): J. Arribas, S. Critelli and M.J. Johnsson, Perspectives from Petrography and Geochemistry. Geological Society of America Special Paper 420, 319-344.

Nishio-Hamane D., Ogoshi Y., Minakiwa T., 2012. Miyahisaite, $(Sr,Ca)_2Ba_3(PO_4)_3F$, a new mineral of the hedyphane group in the apatite supergroup from the Shimoharai mine, Oita Prefecture, Japan. Journal of Mineralogical and Petrological Sciences 107, 121-126.

Olds T.A., Kampf A.R., Rakovan J.F., Burns P.C., Mills O.P., Laughlin-Yurs C., 2021. Hydroxylpyromorphite, a mineral important to lead remediation: Modern description and characterization. American Mineralogist 106, 922-929.

Onac B.P., Effenberger H., Ettinger K., Panzaru S.C., 2006. Hydroxylellestadite from Cioclovina Cave (Romania): Microanalytical, structural, and vibrational spectroscopy data. American Mineralogist 91, 1927-1931.

O'sullivan G., Chew D., Kenny G., Henrichs I., Mulligan D., 2020. The trace element composition of apatite and its application to detrital provenance studies. Earth-Science Reviews 201, 103044.

Parat F., Holtz F., Klügel A., 2011. S-rich apatite-hosted glass inclusions in xenoliths from La Palma: constraints on the volatile partitioning in evolved alkaline magmas. Contributions to Mineralogy and Petrology 162, 463-478.

Pasero M., Kampf A.R., Ferraris C., Pekov I.V., Rakovan J., White T.J., 2010. Nomenclature of the apatite supergroup minerals. European Journal of Mineralogy 22, 163-179.

Pekov I.V., Britvin S.N., Zubkova N.V., Pushcharovsky D.Y., Pasero M., Merlino S., 2010. Stronadelphite, $Sr_5(PO_4)_3F$, a new apatite-group mineral. European Journal of Mineralogy 22, 869-874.

Pekov I.V., Koshlyakova N.N., Zubkova N.V., Krzątała A., Belakovskiy D.I., Galuskina I.O., Galuskin E.V., Britvin S.N., Sidorov E.G., Vapnik Y., Pushcharovsky D.Y., 2022. Pliniusite, $Ca_5(VO_4)_3F$, a new apatite-group mineral and the novel natural ternary solid-solution system pliniusite-svabite-fluorapatite. American Mineralogist 107, 1626-1634.

Pekov I.V., Zubkova N.V., Chukanov N.V., Husdal T.A., Zadov A.E., Pushcharovsky D.Y., 2011. Fluorbritholite-(Y), $(Y,Ca,Ln)_5[(Si,P)O_4]_3F$, a new mineral of the britholite group. Neues Jahrbuch für Mineralogie Abhandlungen 188, 191-197.

Pekov I.V., Zubkova N.V., Husdal T.A., Kononkova N.N., Agakhanov A.A., Zadov A.E., Pushcharovsky D.Y., 2012. Carlgieseckeite-(Nd), $NaNdCa_3(PO_4)_3F$, a new belovite-group mineral species from the Ilímaussaq Alkaline Complex, south Greenland. Canadian Mineralogist 50, 571-580.

Peng G., Luhr J.F., Mcgee J.J., 1997. Factors controlling sulfur concentrations in volcanic apatite. American Mineralogist 82, 1210-1224.

Piccoli P.M. and Candela P.A., 2002. Apatite in Igneous Systems. Reviews in Mineralogy and Geochemistry 48, 255-292.

Pieczka A., Biagioni C., Gołębiowska B., Jele Ń.P., Pasero M., Sitarz M., 2018. Parafiniukite, $Ca_2Mn_3(PO_4)_3Cl$, a new member of the apatite supergroup from the Szklary Pegmatite, Lower Silesia, Poland: Description and crystal structure. Minerals 8, 485.

Qiu K.F., Zhou T., Chew D., Hou Z.L., Müller A., Yu H.C., Lee R.G., Chen H., Deng J., in press. Apatite trace element composition as an indicator of ore deposit types: a machine learning approach. American Mineralogist.

Rakovan J.F. and Hughes J.M., 2000. Strontium in the apatite structure: Strontian fluorapatite and Belovite-(Ce). Canadian Mineralogist 38, 839-845.

Rouse R.C. and Dunn P., 1982. A contribution to the crystal chemistry of ellestadite and the silicate sulfate apatites. American Mineralogist 67, 90-96.

Rukhlov A.S., Plouffe A., Ferbey T., Mao M., Spence J., 2016. Application of trace-element compositions of detrital apatite to explore for porphyry deposits in central British Columbia. In: Geological Fieldwork 2015, British Columbia Ministry of Energy and Mines, British Columbia Geological Survey Paper 2016-1, 145-179.

Schlüter J., Malcherek T., Gebhard G., 2016. Vanackerite, a new lead cadmium arsenate of the apatite supergroup from Tsumeb, Namibia. Neues Jahrbuch für Mineralogie Abhandlungen 193, 79-86.

Sejkora J., Plášil J., Císařová I., Škoda R., Hloušek J., Veselovský F., Jebavá I., 2011. Interesting supergene Pb-rich mineral association from the Rovnost mining field, Jáchymov (St. Joachimsthal), Czech Republic. Journal of Geosciences 56, 257-271.

Środek D., Galuskina I.O., Galuskin E., Dulski M., Książek M., Kusz J., Gazeev V., 2018. Chlorellestadite, $Ca_5(SiO_4)_{1.5}(SO_4)_{1.5}Cl$, a new ellestadite- group mineral from the Shadil-Khokh volcano, South Ossetia. Mineralogy and Petrology 112, 743-752.

Szuszkiewicz A., Pieczka A., Golebiowska B., Dumańska-Slowik M., Marszalek M., Szeleg E., 2018. Chemical composition of Mn- and Cl-rich apatites from the Szklary Pegmatite, central Sudetes, SW Poland: taxonomic and genetic implications. Minerals 8, 350.

Tait K., Ball N.A., Hawthorne F.C., 2015. Pieczkaite, ideally $Mn_5(PO_4)_3Cl$, a new apatite-supergroup mineral from Cross Lake, Manitoba, Canada: Description and crystal structure. American Mineralogist 100, 1047-1052.

Tan H.M.R., Huang X.W., Meng Y.M., Xie H., Qi L., 2023. Multivariate statistical analysis of trace elements in apatite: Discrimination of apatite with different origins. Ore Geology Reviews 153,105269.

Teiber H., Marks M.A.W., Arzamastsev A.A., Wenzel T., Markl G., 2015. Compositional variation in apatite from various host rocks: clues with regards to source composition and crystallization conditions. Neues Jahrbuch für Mineralogie Abhandlungen 192, 151-167.

Vlasáč J., Mikuš T., Ondrejka M., Žitňan P., Tuček P., 2021. Supergene Pb-Cu-(Sb) mineral assemblage in abandoned epithermal deposit Rudno nad Hronom, Slovakia. Acta Geologica Slovaca 13, 107-118.

Wu B., Gu X.P., Rao C., Wang R.C., Xing X.Q., Zhong F.J., Wan J.J., Bonnetti C., 2022. Fluorsigaiite, $Ca_2Sr_3(PO_4)_3F$, a new mineral of the apatite supergroup from the Saima alkaline complex, Liaoning Province, China. Mineralogical Magazine 86, 940-947.

Warr L.N., 2021. IMA-CNMNC approved mineral symbols. Mineralogical Magazine 85, 291-320.

Yavuz F., 2001. PYROX: A computer program for the IMA pyroxene classification and calculation scheme. Computers & Geosciences 27, 97-107.

Yavuz F., 2003. Evaluating micas in petrologic and metallogenic aspect: I-definitions and structure of the computer program MICA+. Computers & Geosciences 29, 1203-1213.

Yavuz F., 2007. WinAmphcal: a windows program for the IMA-04 amphibole classification. Geochemistry, Geophysics, Geosystems 8, Q01004.

Yavuz F., 2013. WinPyrox: A Windows program for pyroxene calculation classification and thermobarometry. American Mineralogist 98, 1338-1359.

Yavuz F. and Yıldırım D.K., 2018. A Windows program for calculation and classification of epidote-supergroup minerals. Periodico di Mineralogia 87, 269-285.

Yavuz F. and Yıldırım D.K., 2020. WinGrt, a Windows program for garnet supergroup minerals. Journal of Geosciences 65, 71-95.

Yavuz F., Karakaya N., Yıldırım D.K., Karakaya M.Ç., Kumral M., 2014. A Windows program for calculation and classification of tourmaline-supergroup (IMA-2011). Computers & Geosciences 63, 70-87.

Yavuz F., Kumral M., Karakaya N., Karakaya M.Ç., Yıldırım D.K., 2015. A Windows program for chlorite calculation and classification. Computers & Geosciences 81, 101-113.

Yavuz F. and Yavuz V., 2023. WinSpingc, a Windows program for spinel supergroup minerals. Journal of Geosciences 68, 95-110.

Yavuz F. and Yavuz V., in press. WinPclcas, a Windows program for pyrochlore supergroup minerals. Canadian Journal of Mineralogy and Petrology.

Zhang H., An F., Ling M., Feng X., Sun W., 2022. Metallogenesis of porphyry copper deposit indicated by in situ zircon U-Pb-Hf-O and apatite Sr isotopes, Minerals 12, 1464.

Zhou T., Cai Y.W., An M.G., Zhou F., Zhi C.L., Sun X.C., Tamer M., 2023. Visual interpretation of machine learning: genetical classification of apatite from various ore sources. Minerals 13, 491.

PM